

# Using extracellular action potential recordings to constrain compartmental models

Carl Gold · Darrell A. Henze · Christof Koch

Received: 8 June 2006 / Revised: 30 November 2006 / Accepted: 26 December 2006 / Published online: 2 February 2007  
© Springer Science + Business Media, LLC 2007

**Abstract** We investigate the use of extracellular action potential (EAP) recordings for biophysically faithful compartmental models. We ask whether constraining a model to fit the EAP is superior to matching the intracellular action potential (IAP). In agreement with previous studies, we find that the IAP method under-constrains the parameters. As a result, significantly different sets of parameters can have virtually identical IAP's. In contrast, the EAP method results in a much tighter constraint. We find that the distinguishing characteristics of the waveform—but not its amplitude—resulting from the distribution of active conductances are fairly invariant to changes of electrode position and detailed cellular morphology. Based on these results, we conclude that EAP recordings are an excellent source of data for the purpose of constraining compartmental models.

**Keywords** Compartmental model · Extracellular recording · Model constraint · CA1 · Pyramidal neuron · Neuron simulation

## 1 Introduction

Compartmental neuron models are one of the most useful computational methods in modern neuroscience. This is be-

cause they allow conjectures based on physiological data to be tested for biophysical plausibility and then generate additional predictions which can be tested by further physiological experiments (for review see e.g. Koch and Segev, 1999; Stuart et al., 2001). A common difficulty with the application of compartmental models is constraining the many parameters controlling their properties (Vanier and Bower, 1999; Keren et al., 2005; Hayes et al., 2005; Huys et al., 2006). This is particularly the case with compartmental models based on complete cell reconstructions and including the variety of ionic channels known to occur on different neuronal cell types and their corresponding non-uniform conductance densities (Migliore and Sheperd, 2002). Such models can easily possess 100 or more degrees of freedom.

A variety of data is used to tune *in vitro* compartmental models, principally membrane potential traces, spike times in response to current injection, and sub-threshold current vs. voltage (I-V) curves (see e.g. Vanier and Bower, 1999; Keren et al., 2005a). However, Keren et al. (2005) found that both membrane potential traces and spike times yield non-optimal performance as the model constraint for a genetic algorithm search. They proposed the additional constraint of the voltage vs. the first derivative of the voltage. Hayes et al. (2005) came to a similar conclusion, arguing for the cumulative voltage integral as a model constraint. Huys et al. (2006) demonstrated that if the membrane potential is known or can be closely estimated for all compartments of a neuron then optimal model parameters can be determined directly. This approach would rely on optical imaging of the membrane potential.

If a modeling study aims to reproduce *in vivo* conditions the choices are more limited by the difficulty of applying these protocols. The most abundant measurements of *in vivo* neuronal activity are extracellular

---

**Action Editor:** Alain Destexhe

---

C. Gold (✉) · C. Koch  
Computation and Neural Systems, California Institute of  
Technology, Pasadena, CA, USA  
e-mail: carlg@caltech.edu

D. A. Henze  
Department of Pain Research, Merck Research Laboratories,  
West Point, PA, USA

recordings. Yet, surprisingly, there have been few attempts to tune compartmental models with this data (Varona et al., 2000). If compartmental models are to be widely used to match *in vivo* conditions, it would be advantageous if there was a practical method to tune them using extracellular recordings in the absence of additional protocols.

We recently performed a detailed simulation study recreating simultaneous intra- and extracellular recordings of CA1 pyramidal neurons *in vivo* (Gold et al., 2006a). Action potentials were simulated based on morphological reconstructions of the recorded cells and the resulting extracellular potentials were calculated based on the membrane currents predicted by the model. We tuned the model parameters for each cell until a plausible match was achieved for both the intracellular action potential (IAP) and the extracellular action potential (EAP). The tuned model allowed detailed explanation of a variety of features of the EAP's. An interesting finding was that variation of cell morphology within the class of CA1 pyramidal neurons made only minimal impact on the EAP waveform, while different distributions of active conductance densities have predictable impacts on the EAP waveform. This finding suggests that EAP's recorded *in vivo* may be used to analyze the intracellular state of the neuron, including active ionic conductance kinetics and conductance densities, the parameters that must typically be tuned when constraining a compartmental model.

In the process of tuning the model we observed that it was significantly easier to tune the model to closely match the IAP waveform than to match the EAP waveform. It has previously been observed that single IAP traces are a weak constraint on the compartmental model (Keren et al., 2005). Our own observations suggest the novel possibility that EAP waveforms may have significantly greater power as a model constraint.

To further investigate this, we analyzed cases where a compartmental model could have significantly different conductance density parameters but still produce the same IAP waveform. For these cases, we analyzed the influence that the conductance density parameters had on the EAP. One potential drawback of using EAP measurements to tune a compartmental model is the sensitivity of the EAP to the position of the measuring electrode: if the position is not known with a high degree of accuracy it may introduce uncertainty which cancels any benefit. Also, if a model is tuned from EAP recordings made *in vivo* then the morphology of the neuron will also be unknown. We addressed these issue by analyzing the sensitivity of EAP features to electrode position and morphological variation as predicted by the model.

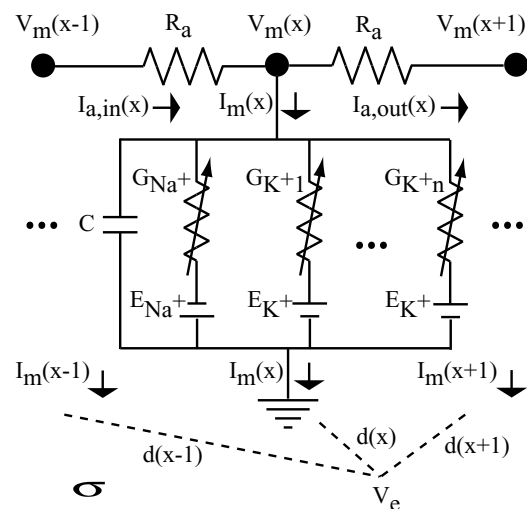


**Fig. 1** Circuit model of intracellular and extracellular potentials

## 2 Methods

### 2.1 Compartmental model simulations

#### 2.1.1 Overview

The standard circuit model for a compartmental model is shown in Fig. 1. The intracellular potential for a typical compartment is derived from current conservation,

$$I_m = I_{a,in} - I_{a,out} \quad (1)$$

The membrane current,  $I_m$ , is given by the sum of the ionic currents, the membrane capacitive current, and any leak current. The axial currents,  $I_{a,in}$  and  $I_{a,out}$ , are given by the difference between the voltage in neighboring compartments divided by the axial resistivity,  $R_a$ , which is assumed here to be constant as would be the case for neighboring compartments of identical size. This leads to the first order differential equation:

$$\begin{aligned} -C \frac{dV_m(x)}{dt} = & G_{Na^+}(x)[V_m(x) - E_{Na^+}] \\ & + \sum_n G_{K+n}(x)[V_m(x) - E_{K^+}] \\ & - \frac{[V_m(x-1) - V_m(x)]}{R_a} \\ & + \frac{[V_m(x) - V_m(x+1)]}{R_a} + \dots \end{aligned} \quad (2)$$

where  $G_{Na^+}$  and the  $G_{K+n}$  are understood to have the usual non-linear voltage-time dependence (see e.g. Koch, 1999), and  $\dots$  refers to leak and  $Ca^{2+}$  conductances which are orders

of magnitude smaller than the  $\text{Na}^+$  and  $\text{K}^+$  conductances during an action potential. We performed our compartmental simulations using the NEURON Simulation Environment (Hines and Carnevale, 1997).

The parameters of the model that must be estimated can include both the passive parameters,  $C$ , and  $R_a$ , as well as the maximum conductance densities and kinetics parameters of the time varying resistances  $G_{\text{Na}^+}$  and the  $G_{\text{K}^+n}$  (usually referred to as  $\bar{g}$ ). In practice the densities of the different conductances vary greatly across different classes of neurons (Migliore and Sheperd, 2002) and even between different cells (Toledo-Rodriguez et al., 2004) while the expected values for the passive parameters are expected to be in a more confined range (Koch, 1999). For this reason we focus our attention on the parameters of the active conductance densities.

### 2.1.2 Active conductances and passive properties

The model includes Hodgkin-Huxley style kinetic models for 15 different voltage and/or  $[\text{Ca}^{2+}]$  dependent ionic conductances known to be present on CA1 pyramidal cells (for review, e.g. Borg-Graham, 1999). Several of the conductances had non-uniform distributions densities as suggested by previous *in vitro* research (for review, e.g. Migliore and Sheperd 2002). The conductances were fast inactivating  $\text{Na}^+$  (somatic and axonal varieties), A type  $\text{K}^+$  (proximal and distal varieties), AHP type  $\text{Ca}^{2+}$  dependent  $\text{K}^+$ , C type voltage and  $\text{Ca}^{2+}$  dependent  $\text{K}^+$ , D type  $\text{K}^+$ , K type  $\text{K}^+$ , M type  $\text{K}^+$ , H type mixed cation (somatic and distal varieties), L type  $\text{Ca}^{2+}$ , N type  $\text{Ca}^{2+}$ , R type  $\text{Ca}^{2+}$ , T type  $\text{Ca}^{2+}$ . The active conductance kinetics were modeled with the formalism of Borg-Graham (1999), with somewhat different parameter choices as detailed in Appendix B of Gold et al. (2006a).

As we focused in this study on reproducing the shape of the EAP, we treated the maximal conductance densities ( $\bar{g}$ ) for the  $\text{Na}^+$  and A, C, D, K and M type  $\text{K}^+$  conductances as variables that could be tuned, leaving the remaining parameters (including the passive parameters and active ionic conductance kinetics) fixed for all simulations. Current due to the  $\text{Ca}^{2+}$ , H and AHP conductances as well as the passive leak were much smaller and consequently do not play a significant role in the generation of the EAP waveform (although  $[\text{Ca}^{2+}]$  plays an important role in the control of the C type  $\text{K}^+$  conductance.) The values used for the tunable conductance densities are listed in Table 3 in Section 3.1, below. The values used for the fixed conductances are the same as those listed in Table C.1, Appendix C, in Gold et al. (2006a). The system of the non-uniform distribution of conductances are also described in Appendix C of Gold et al. (2006a), albeit based on the conductance parameters given in Table 3. The passive parameters and model for spines are the same as described in Appendix A of Gold et al. (2006a).

Synaptic input was mimicked by reducing the leak resistance and assigning a reversal potential above threshold in the compartments receiving synaptic input, as described in Gold et al. (2006a), Methods. Usually the simulated synaptic input was applied to all dendritic compartment  $>50 \mu\text{m}$  from the soma for a short time ( $<5 \text{ms}$ ) until an action potential was initiated. For complete details of the compartmental model (see Gold et al., 2006a).

### 2.1.3 Cell morphologies

The cells used for simulation are reconstructed CA1 pyramidal cells from the experiments described in Henze et al. (2000). Most of the simulations described were performed on a single morphology, while in Section 3.8 we consider results comparing 17 different neuronal reconstructions. The size of the cells in the sample is described in Section 3.8.

The axon for each cell was modeled similar to that described in Mainen et al. (1995): An axon hillock  $10 \mu\text{m}$  long connects the soma to the initial segment which is  $15 \mu\text{m}$  long. After the initial segment the axon consists of five alternating myelinated sections ( $100 \mu\text{m}$  long) and nodes of Ranvier ( $1 \mu\text{m}$  long). The active  $\text{Na}^+$  conductance in the initial segment and nodes of Ranvier is modeled based on the results of Colbert and Pan (2002): it is active at a lower threshold than the active  $\text{Na}^+$  conductance in the soma and dendrites. The  $\text{Na}^+$  conductance in the initial segment has a somewhat higher density than that in the soma. The initial segment repolarizes actively with K and D type  $\text{K}^+$  conductance only, while the nodes of Ranvier repolarize passively. The fifth (final) node terminates with a sealed end.

We also performed simulations of single, long cylinder to analyze the spatial derivatives of the membrane potential in a simplified geometry as described in Section 3.4. These models consisted of 101 compartments, each  $3 \mu\text{m}$  in diameter and  $10 \mu\text{m}$  in length (total length of  $1010 \mu\text{m}$ ). The passive parameters and active conductances were the same as for the detailed morphological reconstructions, although the conductance densities used were slightly modified. The simplified models contained no axon and were excited to action potential by means of a simulated current injection using the standard IC Clamp mechanism provided with the NEURON Simulation Environment (Hines and Carnevale, 1997).

## 2.2 Calculation of model extracellular action potentials

The EAP is calculated in two stages. First, we computed the transmembrane potential and currents for a pyramidal neuron model using the NEURON simulation environment (Hines and Carnevale, 1997). Second, we used those currents to compute the extracellular potentials with the Line Source Approximation (LSA) (Holt and Koch, 1999).

It has been previously demonstrated that the neuropil is well modeled by an isotropic volume conductor and that the electric potential in the extracellular space is governed by Laplace's equation (Plonsey, 1969). For a single point source in an unbounded isotropic volume conductor, the solution is dual to the classical physics problem of point charges in free space (Coulomb's law):

$$V_e = \frac{I}{4\pi d\sigma} \quad (3)$$

where  $I$  is amplitude of a point source of current (A), and  $d$  is the distance from the source to the measurement (m), and  $\sigma$  is the conductivity (S/m) of extracellular space (we assume  $\sigma = 0.3$  S/m, or  $R_e = 333 \Omega\text{cm}$ ).

For intuition purposes, a simplified (point source) model for the extracellular potential resulting from a multi-compartment model is given by:

$$\begin{aligned} V_e &\approx \frac{1}{4\pi\sigma} \sum_x \frac{I_m(x)}{d(x)} \\ &\approx \frac{1}{4\pi\sigma} \sum_x \frac{1}{d(x)} \left\{ G_{\text{Na}^+}(x)[V_m(x) - E_{\text{Na}^+}] \right. \\ &\quad \left. + \sum_n G_{\text{K}^+n}(x)[V_m(x) - E_{\text{K}^+}] + C \frac{dV_m(x)}{dt} \right\} \quad (4) \end{aligned}$$

as illustrated in Fig. 1. In practice such an approximation would give inaccurate results if the compartment size were not extremely fine.

The LSA uses a simplified continuous distribution of membrane currents by locating the net current for each neurite on a line down the center of the neurite. The current for each compartment is distributed over the three dimensional line segments (from the morphological reconstruction) that it spans. By assuming a line distribution of current the resulting potential has a straightforward analytic solution (Holt, 1998; Holt and Koch, 1999). For a single linear current source having length  $\Delta s$ , the resulting potential is given by:

$$\begin{aligned} V_e &= \frac{1}{4\pi\sigma\Delta s} \int_{-\Delta s}^0 \frac{I ds}{\sqrt{r^2 + (h-s)^2}} \\ &= \frac{I}{4\pi\sigma\Delta s} \log \left| \frac{\sqrt{h^2 + r^2} - h}{\sqrt{l^2 + r^2} - l} \right| \quad (5) \end{aligned}$$

where  $r$  is the radial distance from the line,  $h$  is the longitudinal distance from the end of the line, and  $l = \Delta s + h$  is the distance from the start of the line. Holt (1998) and Holt and Koch (1999) analyzed the accuracy of the the LSA and found it to be highly accurate in comparison to a continuous cylindrical distribution, except at very close distances

(i.e.  $\sim 1 \mu\text{m}$ ) to the cable. Because extracellular recording electrodes are typically many  $\mu\text{m}$ 's away from neurons, we can use the LSA to calculate extracellular potentials from a model with high accuracy regardless of the interior compartmentalization of the model neuron.

This approach assumes that the extracellular medium is a homogeneous and isotropic volume conductor. We are therefore not considering the fact that the CA1 region is in fact inhomogeneous (López-Aguado et al., 2001), although the impact of this inhomogeneity is not great, as discussed in Gold et al. (2006a). This approach also does not analyze filtering effects that may be caused by the extracellular medium, as suggested in Bedard et al. (2006).

### 2.3 Comparison of model currents

In order to facilitate comparison of membrane and axial currents in compartments of unequal sizes we present current data for the reconstructed neuron *normalized* to a fixed compartment size of  $10 \mu\text{m}$  length and  $2.5 \mu\text{m}$  diameter. Membrane current is normalized by a factor of  $N_m = S_{\text{actual}}/S_{\text{standard}}$ , where  $S$  is the membrane surface area of the compartment. Axial currents are normalized according to  $N_a = C_{\text{actual}}/C_{\text{standard}}$  where  $C$  indicates the compartment cross sectional area. Table 1 lists the compartments used for comparison, their actual size and the normalization factor used in converting their currents to the equivalent "standard" size compartment. Table 1 also lists the number of compartments ("Nsegs") in the same unbranched length of neurite as the compartment that is presented for analysis. Because neighboring compartments in the model have nearly identical active conductances they will make virtually identical contributions to the nearby extracellular potentials.

### 2.4 Comparison of EAP waveforms

To compare intra- and extra-cellular spike shapes across models, we computed the minimum normalized square root of the mean square error (SMSE) between aligned waveforms. To calculate the SMSE, the waveforms are first interpolated to a regular sampling of 20,000 Hz from the variable step integration used for the simulations (Hines and Carnevale, 2001).

The peak amplitude of the EAP waveform is of particular interest because of its close relationship to the  $\text{Na}^+$  conductance density, but the brief duration of the EAP peak means a mismatch at the peak will make only a small contribution to an unweighted error measure. To remedy this, we weighted the error at the peak amplitude sample by a factor of 10 and the error at the surrounding samples by factors of 5, 2.5, and 1.25 respectively (all other samples received a weight of 1) and then normalized the resulting error. In calculating

**Table 1** Comparison of Model Compartments For comparison in Figs. 4–7 membrane currents,  $I_m$ , and axial currents,  $I_a$  are multiplied by the normalization factors  $N_m$  and  $N_a$  respectively. Normalization

factors are calculated from the ratio of the surface area,  $S$ , and cross sectional area,  $C$ , in comparison to the standard compartment size. Nsegs gives the total number of compartments in the same section

Compartment	Length ( $\mu\text{m}$ )	Diameter ( $\mu\text{m}$ )	Area ( $\mu\text{m}^2$ )		$N_m$	$N_a$	Nsegs
			S	C			
Standard	10	2.5	78.5	4.9	1	1	1
Soma	18.8	9.5	560	71	0.14	0.07	1
Axon Initial Segment	3.0	0.67	6.3	0.35	12.46	13.9	5
Apical Trunk @ 25 $\mu\text{m}$	16.8	3.2	169	8.04	0.46	0.61	3
Apical Trunk @ 100 $\mu\text{m}$	8.0	2.0	50.5	3.14	1.55	1.56	3
Apical Trunk @ 200 $\mu\text{m}$	10.7	2.0	67	3.14	1.17	1.56	5

the error on a 4 ms waveform this method gives roughly 27% of the weight to the 9% of the sample points centered around the peak. For consistency, the same method was applied to the IAP waveforms, although the longer duration of the peak meant that the weighting method was relatively less consequential.

The waveforms were voltage offset and shifted in time in order to determine the minimal SMSE. Samples of a waveform being shifted enter and leave the comparison window while the other waveform stays constant, making the measure asymmetric. To remedy this we calculated the error between two waveforms twice, shifting each in turn, and took the average of the two errors. Finally, the SMSE is normalized by the peak amplitude (of the smaller of the two waveforms) to enable comparison of errors on the IAP and the EAP and on EAP's with different amplitude.

### 2.5 Measurement of EAP waveform features

We measured the features of the EAP waveforms produced by the model as illustrated in Fig. 2. We focused on 7 measures:

1. The amplitude of the initial, positive peak associated with the capacitive current (if present).

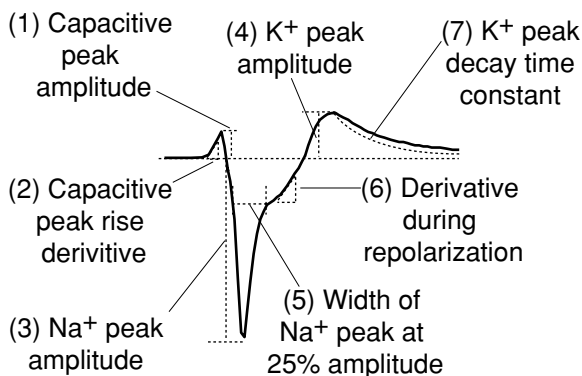


**Fig. 2** Measurements of EAP waveforms

2. The first derivative of the waveform in the rising phase to the capacitive peak. The derivatives are approximated simply as  $\Delta V / \Delta t$  at each (inhomogeneous) time step in the simulation.
3. The amplitude of the large, negative peak due to the  $\text{Na}^+$  current.
4. The amplitude of the positive peak following the negative peak from the combined repolarizing  $\text{K}^+$  current (if present).
5. The width (duration) of the  $\text{Na}^+$  peak measured at 25% of peak amplitude.
6. The first derivative during the repolarization phase of the  $\text{Na}^+$  peak. The repolarization phase is defined as the portion of the waveform between the (negative)  $\text{Na}^+$  peak, including the first 2/3 of the samples until the  $\text{K}^+$  peak (or the end of the waveform if there is no  $\text{K}^+$  peak).
7. The decay time constant of the  $\text{K}^+$  peak. For waveforms with no  $\text{K}^+$  peak (no local maxima in the EAP after the negative  $\text{Na}^+$  peak), the exponential is fit to the final 1/3 of the samples between the  $\text{Na}^+$  peak and the end of the window; the negative value resulting from the fit for the exponent indicates that the waveform is increasing during this window.

Because of the decay in the amplitude of the waveform with increasing distance from the neuron, as described in Section 3.7, we normalize the amplitude of the capacitive and  $\text{K}^+$  peaks by that of the  $\text{Na}^+$  peak and interpret them as a percentage. The amplitude of the  $\text{Na}^+$  peak is not used as a feature by itself.

EAP's were calculated on a  $50 \times 50 \mu\text{m}$  grid in the plane of the soma and apical trunk at a spacing of  $10 \mu\text{m}$ . We considered only waveforms with peak amplitude  $> 40 \mu\text{V}$ . The required amplitude for detection and clustering EAP's in CA1 is around  $60 \mu\text{V}$  (Henze et al., 2000) and we have observed a similar threshold in cortical recordings (Gold et al., 2006b). We have chosen the somewhat lower threshold of  $40 \mu\text{V}$  for these tests because the level of background noise in extracellular recordings is highly dependent

**Table 2** Measure of between trial difference. The error measure is expressed as a percentage, the normalized square root of the mean square error (NSMSE), as described in Section 2.4. The location of the measurements are the same as those compared in Fig. 3 and detailed in Figs. 4–7

Trials	Intracellular			Extracellular		
	Soma	Apical Trunk, 100 $\mu\text{m}$	Apical Trunk, 200 $\mu\text{m}$	$x = 0 \mu\text{m}$ , $y = 20 \mu\text{m}$	$x = 50 \mu\text{m}$ $y = 30 \mu\text{m}$	$x = 100 \mu\text{m}$ , $y = 40 \mu\text{m}$
A/B	3.2	7.1	45.8	8.3	7.1	17.7
A/C	2.7	4.7	30.1	17.8	14.1	26.5
A/D	3.2	11.1	53.1	15.6	9.4	25.4
B/C	3.6	4.9	29.8	16.8	17.3	20.7
B/D	2.8	7.1	27.9	10.1	5.5	14.7
C/D	2.8	10.0	57.2	18.1	17.1	16.7
Average	3.1	7.5	40.7	14.5	11.8	20.3

on the recording equipment and setup. Our previous results (Gold et al., 2006a) suggested that lower amplitude waveforms will be more varied in shape. Consequently we felt it best to err on the side of caution by including waveforms that may be detectable with a very low noise configuration. In that way our analysis in Section 3.7 presents a greater range of variability in waveform shape than may be commonly observed.

### 3 Results

#### 3.1 Dependence of EAP waveform on active conductance distributions

In order to analyze how the EAP waveform depends on the density of active ionic conductances we created a small number of simulations with significantly different active conductance densities but with very similar IAP's at the soma. Forcing the simulations to have (nearly) identical IAP's illustrates the different way in which intracellular and extracellular potentials are generated. Parameters were tuned manually and the results for four simulations are shown in Fig. 3. For the four simulations, the IAP's are virtually indistinguishable at the soma and remain very similar at a location on the apical trunk 100  $\mu\text{m}$  from the soma. Only beyond 200  $\mu\text{m}$  from the soma do the differences between the four simulations becomes apparent. Yet the four simulations produce very different EAP's at three measurement locations near the soma and along the apical trunk (Table 2).

The conductance densities used for the simulations are shown in Table 3. The main features of the four simulations are as follows: (A) The axon initial segment has a significantly larger  $\text{Na}^+$  conductance density than the soma, in comparison to the simulations (B–D), and repolarization depends primarily on the C type  $\text{K}^+$  conductance; (B) repolarization depends primarily on the K type  $\text{K}^+$  conductance; (C) repolarization depends primarily on the A type  $\text{K}^+$  conductance; (D) similar to (B), except that the  $\text{Na}^+$  conductance

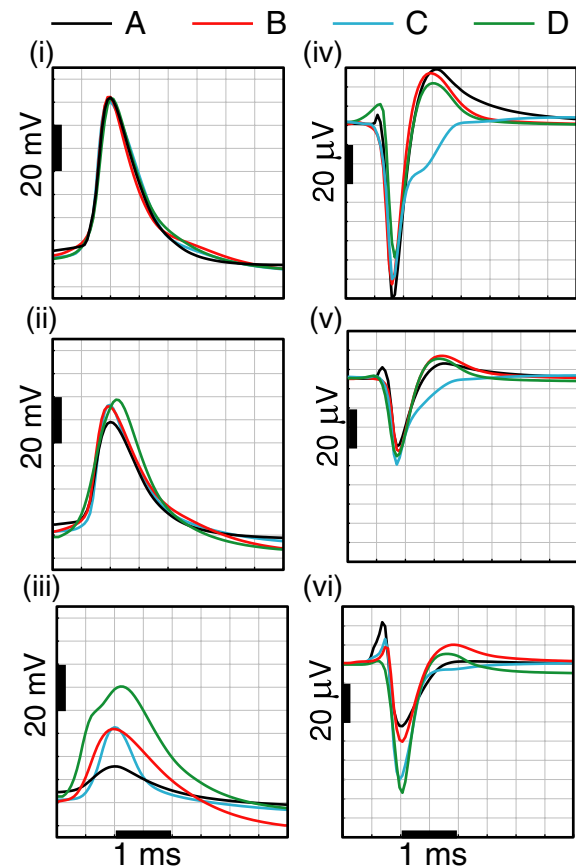


**Fig. 3** Comparison of Intra and Extracellular Action Potentials for four conductance density models. *Left column*: IAP at the soma (i), and on the apical trunk at 100 (ii) and 200  $\mu\text{m}$  (iii). The IAP's at the soma are virtually indistinguishable, and the difference does not become significant until the measurement at 200  $\mu\text{m}$ . *Right column*: EAP measurements near the soma (iv), near the apical trunk 50  $\mu\text{m}$  (v), and near the apical trunk 100  $\mu\text{m}$  from the soma (vi). The EAP's produced by the four simulations are significantly different at all locations. The pairwise error between the simulations are listed in Table 2

density is uniform in the dendrites (whereas in (A–C) the density decreases with distance in the dendrites) and the cell is stimulated only in distal compartments ( $>500 \mu\text{m}$  from the soma) so that the action potential initiates in the distal apical trunk rather than in the axon.

**Table 3** Above: Maximal conductance densities ( $\bar{g}$ ) for the four simulations. All numbers are in units of mS/cm<sup>2</sup>. \* indicates  $\bar{g}$  100  $\mu$ m from the soma—distal sections have densities that are several times greater (Gold et al., 2006a)

Conductance	Maximal conductance, $\bar{g}$ mS/cm <sup>2</sup>			
	A	B	C	D
I <sub>Na</sub> <sup>+</sup> Soma	37.5	36	32.5	20
I <sub>Na</sub> <sup>+</sup> Iseg	450	72	130	20
I <sub>Na</sub> <sup>+</sup> Dend <sub>max</sub>	18.75	23.4	29.25	20
I <sub>Na</sub> <sup>+</sup> Dend <sub>min</sub>	3.75	7.2	22.75	20
I <sub>K</sub> <sup>+</sup> AProx	5	1	50	0.5
I <sub>K</sub> <sup>+</sup> ADist*	10	1	50	0.5
I <sub>K</sub> <sup>+</sup> ADist Basal*	20	2	250	0.5
I <sub>K</sub> <sup>+</sup> ADist Oblique*	20	2	300	0.5
I <sub>K</sub> <sup>+</sup> ADist Tuft*	30	2	400	0.5
I <sub>K</sub> <sup>+</sup> C Soma	25	0.5	5	0.5
I <sub>K</sub> <sup>+</sup> C Dend	18.75	0.25	3.75	0.25
I <sub>K</sub> <sup>+</sup> D	15	2.5	2	2.5
I <sub>K</sub> <sup>+</sup> K	20	40	2	40
I <sub>K</sub> <sup>+</sup> M	1	4.5	1	4.5

As described in Gold et al. (2006a) manual tuning of the parameters was guided by three principles: (1) the net Na<sup>+</sup> conductance for the perisomatic region (including the axon initial segment) is tuned to determine the peak amplitude of the IAP and the EAP; (2) K<sup>+</sup> conductance densities dominant in the perisomatic region (primarily C and K type) are tuned to determine the shape of the K<sup>+</sup> dominant phase of the EAP waveform; (3) K<sup>+</sup> conductances dominant in the distal sections (primarily A, D and M type) are tuned so the IAP repolarizes at the desired rate. Based on these principles we had little difficulty engineering the four simulations to have nearly identical IAP's at the soma despite the significant differences in the conductance densities.

Details of the model for the simulations of Fig. 3 are shown in Figs. 4–7. In each simulation the extracellular waveforms at positions near the soma and along the apical trunk around 50  $\mu$ m and 100  $\mu$ m from the soma (Figs. 4(ii), 5(ii), 6(ii) and 7(ii)) are almost exactly rescaled versions of the net currents for the soma and sample apical trunk compartments close to the measurement sites (Figs. 4(i), 5(i), 6(i) and 7(i), bottom row). As will be discussed further in Section 3.3, the extracellular potential described by Eqs. (3) and (4) is dominated by the most proximal parts of the neuron.

The first difference between the EAP's is in the positive peak due to capacitive current at the start of the EAP waveform. For (A) the capacitive peak is evident at all positions, while in (B) and (C) the capacitive peak is only visible in the most distal EAP. For (D), the capacitive peak is clearly observable only at the location closest to the soma. As described in Gold et al. (2006a), capacitive current appears in the EAP when the section proximal to the electrode is strongly depolarized by axial cur-

rent from another section. For (A), the axon initial segment has a much higher density of Na<sup>+</sup> conductance than the soma while the difference is more modest for (B)–(D) (12 $\times$  and 2–3 $\times$  the somatic value respectively, see Table 3). Consequently, in (A), the spike initiates more strongly in the axon and the initial depolarization of the soma results from axial currents originating in the axon: note the large positive peak at the beginning of the inward axial current for the soma in (A) (Fig. 4(i) 3rd row). In (B) and (C) the somatic and axonal initiation is more nearly simultaneous and the capacitive current at the soma is masked by simultaneous Na<sup>+</sup> current (Figs. 4(i)–6(i), 4th row.)

In (D) (Fig. 7), the action potential initiates in the distal dendrites and then propagates to the soma, resulting in a capacitive peak that is larger than that of (A) but only in the region of the soma. In this case the soma is initially depolarized by axial current from the apical trunk. The capacitive peaks of (A) and (D) can be further distinguished by whether the rise to the peak is abrupt, as in (A), or gradual, as in (D). This is related directly to the abruptness with which the AP begins, as can be seen in the first millisecond of Fig. 3(i). However, the difference between the EAP's of Fig. 3(iv) provides a larger error signal with which to tune a model. These observations show that the presence or absence of a capacitive peak near the soma and its shape are useful measurements for constraining the relative Na<sup>+</sup> conductance densities in the soma, axon and dendrites and for determining the site of AP initiation. One weakness of this approach is that capacitive peaks similar to that of (A) are produced near to the apical trunk following a somatic AP initiation (Buzsáki and Kandel, 1998; Gold et al., 2006a), as illustrated in Fig. 3(vi) (trace (C) and (D)).

A second difference in the measured EAP's is the amplitude of the main negative peak—this is determined by two factors: The first is the density of the Na<sup>+</sup> conductance, which is similar for the the four simulations. A second factor is the density of fast repolarization conductance, particularly the A and K type K<sup>+</sup> conductances, which counteract the peak Na<sup>+</sup> current (see Figs. 4(i)–7(i), 2nd and 4th rows for the time course of the K<sup>+</sup> conductances and the Na<sup>+</sup> and K<sup>+</sup> components of the membrane current). Thus, (B–D), which have higher densities of fast K<sup>+</sup> conductances than (A) have somewhat smaller negative peaks in the EAP near the soma. This suggests that using the amplitude of the EAP peak near the soma may not satisfactorily constrain the Na<sup>+</sup> conductance density, without a means to constrain the A and K type K<sup>+</sup> conductances. However, the density of K<sup>+</sup> conductances is further constrained by the shape of the final positive peak of the EAP waveform. For the *in vivo* case, the amplitude of the negative peak is also made ambiguous by uncertainty about the morphology and electrode position as discussed in Sections 3.7 and 3.8.

The shape of the waveform during the repolarization phase is determined by which K<sup>+</sup> conductances dominate in the

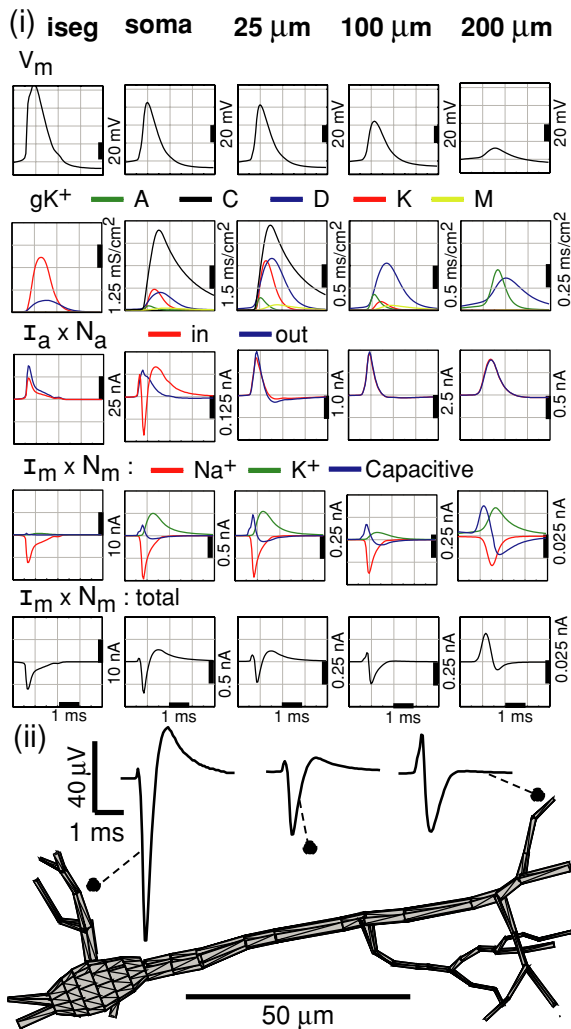


**Fig. 4** Details of simulation (A). (i) Intracellular details. Each column shows data from a single compartment: Axon Initial Segment (iseg), Soma, and apical trunk compartments 25, 100 and 200  $\mu\text{m}$  distance from the soma. *First row*: Membrane potential. *Second row*: Time course of the conductance density for the various types of  $\text{K}^+$  conductances. *Third row*: Normalized axial currents flowing into (i.e. from the direction of the basal dendrites and axon) and out of (i.e. towards the distal apical dendrites) for each compartment. See Section 2.3 for details of normalization procedure. All compartments obey  $I_m = I_{in} - I_{out}$ . The notation agrees with that of Fig. 1, although note that the soma has multiple compartments to the left: the axon and all basal dendrites (not shown). *Fourth row*: Breakdown of the membrane current into  $\text{Na}^+$ ,  $\text{K}^+$  and capacitive components. The membrane current is normalized for compartment size, as described in Section 2.3. *Fifth row*: Normalized total membrane current. (ii) Extracellular potentials at the indicated positions, the same positions compared in Fig. 3 and Table 2. (A) has a high density of  $\text{Na}^+$  conductance in the axon initial segment in comparison to (B) and (C), and the C type  $\text{K}^+$  conductance is dominant in the repolarization. As a result, a large positive capacitive peak is visible in the EAP near the soma, before the negative  $\text{Na}^+$  peak. This is due to the soma being driven by axial current from the axon before the somatic  $\text{Na}^+$  conductance fully activates. The  $\text{K}^+$  dominant positive phase at the end of the EAP has a relatively slow decay due to the slow inactivation of the C current

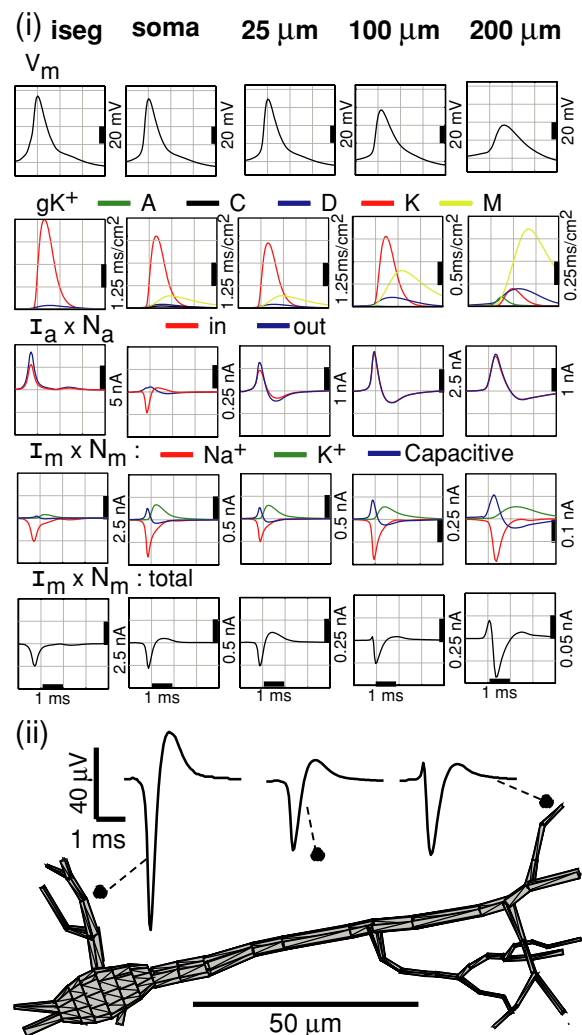


**Fig. 5** Details of simulation (B). For general description see Fig. 4. The simulation has similar  $\text{Na}^+$  conductance densities in the axon and soma and the repolarization is dominated by K type  $\text{K}^+$  conductance. As a result, the positive capacitive dominant peak in the EAP manifests only near the distal apical dendrite which is driven by axial current from the soma and axon. The  $\text{K}^+$  dominant peak of the EAP decays quickly because the K type  $\text{K}^+$  conductance deactivates as soon as the membrane potential repolarizes. Due to the strong repolarizing current produced by the K conductance the axial current shows a reversal as the soma and apical trunk contribute to the repolarization of more distal dendrites

repolarization close to the electrode (see Figs. 4(i)–7(i), 2nd row). In (A) the repolarization is dominated by the C type  $\text{K}^+$  conductance, which is restricted to the soma and the proximal dendrites. The C conductance is  $\text{Ca}^{2+}$  dependent and consequently has a slow decay time, leading to the slower decay of the repolarization phase of the proximal EAP for (A). In (B) and (D), the dominant  $\text{K}^+$  conductance is the K type with a secondary contribution from the M type. The K type  $\text{K}^+$  conductance is uniform throughout the cell, but

has high  $V_m$  threshold for activation making it most active proximal to the soma where the IAP peak is the highest. The K type  $K^+$  conductance de-activates as soon as the IAP is complete, leading to the short duration of the repolarization phase in the EAP's of (B) and (D). In (C), the repolarization is dominated by the A type conductance which has a higher density in distal dendrites. Consequently the EAP proximal to the soma shows no significant  $K^+$  dominant phase.

### 3.2 Axial currents and the membrane potential

The differential equation for  $V_m$ , Eq. (2), contains both membrane and axial current contributions. If the membrane current contribution due to active conductances can be different but the resulting  $V_m(t)$  is the same then the axial current must make up the difference. As illustrated in Figs. 4(i)–7(i), 3rd row, the axial currents are in fact much larger than the membrane current in all compartments except the soma and axon initial segment.

The soma is mainly a source of current to the apical dendrites throughout simulations (A)–(C). The initial positive spike in inward axial current at the soma is due to current flowing from the axon, while at the peak of the somatic AP current is pushed into the basal dendrites (not shown) producing the negative spike in the inward current to the soma (negative according to the sign convention of Fig. 1). During the depolarization phase of the AP the apical trunk compartments shown are also sourcing axial current to more distal compartments (not shown.)

The behavior during repolarization is different for each simulation: in simulations (A) and (B), the soma and proximal apical trunk have significant repolarizing currents due to proximally activated  $K^+$  conductances which leads to the reversal of the axial current in the apical trunk: the soma is contributing to repolarization of the distal dendrites. This is more the case in (B), Fig. 5(i) than in (A), Fig. 4(i). In (C), Fig. 6(i), the net repolarizing current in the perisomatic region is much smaller and distal compartments are self-repolarizing through the local A type  $K^+$  conductances. Consequently there is almost no reversal of axial currents, only a slowing of the outward axial current (which is never as large as in (A) and (B)). Simulation (D), in which the AP initiates in the distal dendrites, is approximately the reverse of (B): axial current flows inward from the apical dendrites to the soma and then reverses during the repolarization phase.

As a result of the large axial currents, the IAP in any given compartment is shaped by the pattern of activity over the entire cell. The depolarization at the soma is created from the pooled  $Na^+$  current from the soma, axon and dendrites.  $K^+$  conductances which are active in distal sections like the A and M type can make a significant contribution to repolarization even at the soma. Of course, axial currents merely reflect differences in  $V_m$  between different compartments, or

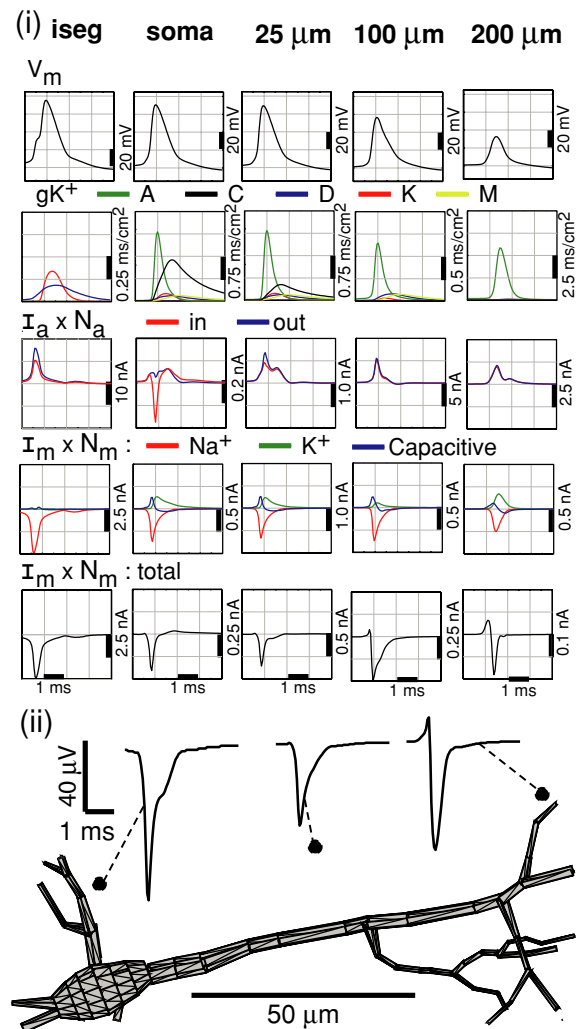


**Fig. 6** Details of simulation (C). For general description see Fig. 4. The simulation has similar  $Na^+$  conductance densities in the axon and soma and the repolarization is dominated by A type  $K^+$  conductance which is most dense in the distal dendrites. As a result, much of the repolarizing current is provided by the distal dendrites and the EAP shows virtually no  $K^+$  dominant phase. The inactivation of the A conductance occurs when the  $Na^+$  conductance is still active, creating an inflection point in the repolarization of the EAP

taken collectively they can be seen as resulting from the spatial gradients in  $V_m$ . However it is viewed, the dependence of the IAP on the overall pattern of activation seems to give it additional degrees of freedom in comparison to the EAP.

### 3.3 $V_m$ Compared to $V_e$ as a model constraint

Inspection of Eqs. (2) and (4) suggests that both  $V_m$  and  $V_e$  introduce possible confounding factors if they are used to estimate the active conductance densities in a model. The membrane potential,  $V_m$ , is made ambiguous by the contribution of both the local membrane current and axial currents from other compartments. As described in Section 3.2, the

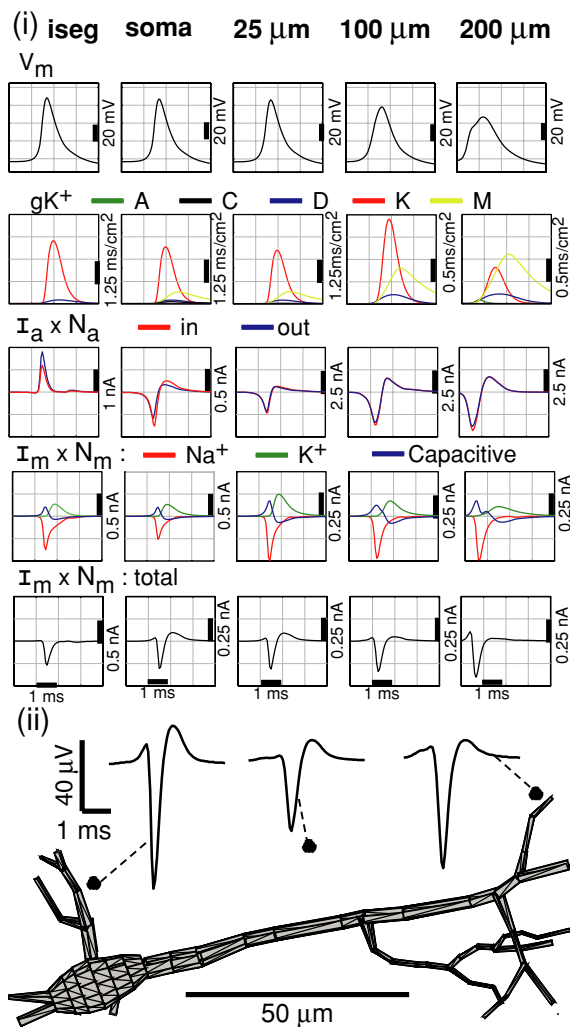


**Fig. 7** Details of simulation (D). For general description see Fig. 4. The  $Na^+$  conductance density is uniform throughout the soma and dendrites and the simulated synaptic input is concentrated in the distal dendrites. Consequently the action potential initiates in the distal apical dendrites and then propagates to the soma. The resulting axial currents in the apical trunk are the inverse of simulation (B), with the distal dendrites first sourcing current to and then sinking current from the perisomatic region. As a result the capacitive dominant peak of the EAP is most visible near the soma and basal dendrites. The  $K^+$  conductances are similar to those of (B) leading to a fast decay of the  $K^+$  dominant phase of the EAP

axial currents are large relative to the membrane currents and reflect the *overall* pattern of activation in the neuron. Consequently different overall distributions of active membrane currents can lead to very similar  $V_m$  waveforms in any given compartment.

The extracellular potential,  $V_e$ , is made ambiguous by the summation of membrane current contributions from multiple compartments at different (possibly unknown) distances. However, in realistic neuron models the active conductance densities in neighboring compartments and the resulting total membrane current,  $I_m(x)$ , is quite similar for neighbor-

ing compartments. Furthermore, the distance dependence for contributions to the extracellular potential is such that compartments that are more than a few tens of microns from the measurement site make little contribution (Gold et al., 2006a). Therefore, for the purposes of intuition the extracellular potential equation may be approximated as

$$V_e \approx \frac{a \langle I_m \rangle_{proximal}}{4\pi\sigma(\langle d \rangle_{proximal})^b} \quad (6)$$

where  $\langle \dots \rangle_{proximal}$  indicates averaging over the most proximal compartments to the recording site. The scaling constant  $a$  accounts for the number and size of neighboring compartments. The constant exponent for the distance term in the denominator,  $1 < b < 3$ , accounts for the fact that in reality the net membrane current for the whole cell is zero and decay will be somewhat faster than inversely proportional to distance, as discussed in detail in Section 3.7.<sup>1</sup>

Equation (6) says that  $V_e$  at a given location will be in direction proportion to the typical  $I_m$  in the most proximal portion of the cell. This makes it depend very directly on the conductance density parameters that we are interested in estimating. Given this constraint on the conductance densities proximal to the electrode, the conditions of biological plausibility and facts provided by studies performed *in vitro* extend the usefulness of the constraint to the entire neuron. For example, conductance densities are expected to vary smoothly with location on the neuron and the density of the A type  $K^+$  current should be much greater in the distal dendrites than the soma (Hoffman et al., 1997). The examples (A–D) all obey these and other similar conditions.

In contrast, we have seen that  $V_m$  measured in a single compartment (typically the soma) is not even a good constraint for the conductance densities in that portion of the cell because it depends so strongly on the overall pattern of activity in the neuron. Consequently a model tuned to match a single  $V_m$  measurement effectively has additional degrees of freedom in comparison to a model tuned to match  $V_e$ . This is true even when using conditions of biological plausibility and facts from *in vitro* studies as additional constraints.

Our examples suggest that this is true despite the fact that  $I_m$  is in fact a function of  $V_m$ . In the case of the  $Na^+$  current channel inactivation makes the  $Na^+$  conductance relatively decoupled to the details of  $V_m$ : as long as a reasonable size action potential occurs the  $Na^+$  conductance will open and then close over the same time course. Variation in the  $V_m$  peak will only change the driving force for a brief period. This is also true of the A current which inactivates on a time scale similar to the  $Na^+$  conductance. The other  $K^+$  conductances (C, D, K and M type), on the other hand,

<sup>1</sup> The constant  $a$  must have units of  $m^{(1-b)}$  to render Eq. (6) dimensionally consistent.

do not inactivate and they are extremely sensitive to the precise peak amplitude and duration of the action potential. However, the ways in which they vary are similar, so that for any typical AP they can still be distinguished. For example, a higher  $V_m$  peak will increase both the C type and K type  $K^+$  conductance and which is dominant may still be judged by the decay time of the  $K^+$  peak in the EAP, as described in Section 3.1.

### 3.4 The relationship between $V_m$ and $V_e$

By combining Eqs. (1) and (2) with Eq. (4) we can actually write the point source approximation for the extracellular potential as a function of the axial currents instead of the membrane currents:

$$V_e = \frac{1}{4\pi\sigma} \sum_x \frac{1}{d(x)} \frac{[V_m(x-1) - 2V_m(x) + V_m(x+1)]}{R_a}$$

Recalling the simplest central difference approximation for the second Derivative (accurate to within  $O(h^2)$ ),

$$f''(x) = (1/h^2)[f(x-h) - 2f(x) + f(x+h)]$$

we can write the equation for  $V_e$  in terms of the second derivative of  $V_m$ :

$$V_e = \frac{l^2}{4\pi\sigma R_a} \sum_x \frac{V_m''(x)}{d(x)} \tag{7}$$

where  $l$  is the compartment length, assumed to be uniform as is the intra-compartment resistance,  $R_a$ . This shows that the extracellular potential at any location is proportional to a weighted sum of the second derivatives of the membrane potential with respect to position.

The proportionality of  $V_e$  to the  $V_m''(x)$  is more concise than describing  $V_e$  in terms of active membrane currents, but the connection to the active conductance densities is obscured. This relationship is exact for all types of membrane currents, in contrast to the approximation that  $V_e$  is proportional to the first time derivative of the membrane potential,  $V_m'(t)$ , as it would be for a passive membrane. The relationship between the extracellular potential and the second derivative of the membrane potential has been previously noted in the literature although its implications for model tuning have not been analyzed; see e.g. (Malmivuo and Plonsey, 1995) where a continuous formulation is derived.

The second derivative of any function highlights regions of rapid change and for this reason forms the basis of many edge detection algorithms in image processing (see e.g. Forsyth and Ponce, 2003). At the presence of an ‘‘edge’’, or as an action potential moves past a particular location, the second derivative goes positive, returns to zero and then

goes negative: the center of the edge coincides with the zero crossing of the second derivative.

In Figs. 8–10 we illustrate the membrane potential and its derivatives as a function of position in simulations of long, single cylinders with parameters tuned to be similar to those of simulations (B), (C) and (D) of Section 3.1.<sup>2</sup> In the simulation based on (B), the action potential initiates at the center and propagates fully to both ends of the cylinder, Fig. 8(ii). In contrast, in the simulation based on (C) the action potential initiates in the center but fails to propagate fully, Fig. 9(ii). In the simulation based on (D) the action potential initiates at one end of the cylinder and propagates to the other end, Fig. 10(ii). Despite these very different spatio-temporal patterns of  $V_m$ , we show that  $V_m(t)$  in a central compartment can be nearly the same: The average NSME for  $V_m$  measured at the center of the cylinders is less than 3% (Figs. 8–10, (i)).

Comparing Figs. 8–10 we observe that  $V_e$  is negative when a local peak in  $V_m(x)$  occurs near the recording location (i.e. the second derivative test for a local maximum). This corresponds to the activation of the  $Na^+$  conductance. A positive  $V_e$  occurs when there is a local minimum in  $V_m(x)$ . This would be the case when an AP initiates in the center of the neuron (the soma) and spreads outwards followed by the center leading in the repolarization, corresponding to the activation of the repolarizing  $K^+$  conductances.

Alternatively, if the AP initiates far from the location of the  $V_e$  measurement and then passes the measurement location the situation is analogous to edge detection in image processing: as the slope increases second derivatives become positive, corresponding to a positive capacitive phase of the EAP. The mid point of the rising slope in  $V_m(x)$  corresponds to a zero crossing of the second derivative and the beginning of the negative,  $Na^+$  dominant phase of the EAP (a local maximum in  $V_m(x)$ ). As the EAP passes the measurement location the falling slope of  $V_m(x)$  will produce a second zero crossing and positive second derivatives corresponding to activation of the  $K^+$  conductances near the recording site.

As  $V_e$  depends on the second spatial derivatives of  $V_m$  it is much more sensitive to the overall pattern of activation than  $V_m$  itself, even when measured only at a single point. Consequently the resulting  $V_e$  waveforms have features which clearly distinguish the different processes at work in each simulation. Figures 8(v)–10(v), showing  $\frac{1}{d(x)} \frac{d^2V_m}{dx^2}$ , clearly illustrate the extent to which  $V_e$  is dominated by contributions from the most proximal regions of the cell. Nevertheless, the weighted average of second derivatives measured from the central sections of the cylinder are informative about the overall pattern of activation. In this light

<sup>2</sup> The result of simulation (A) relies on an additional axonal cylinder and so it is less suitable for this simplified experiment. The conclusions derived from the (D) type cylinder are also applicable to the (A) scenario.

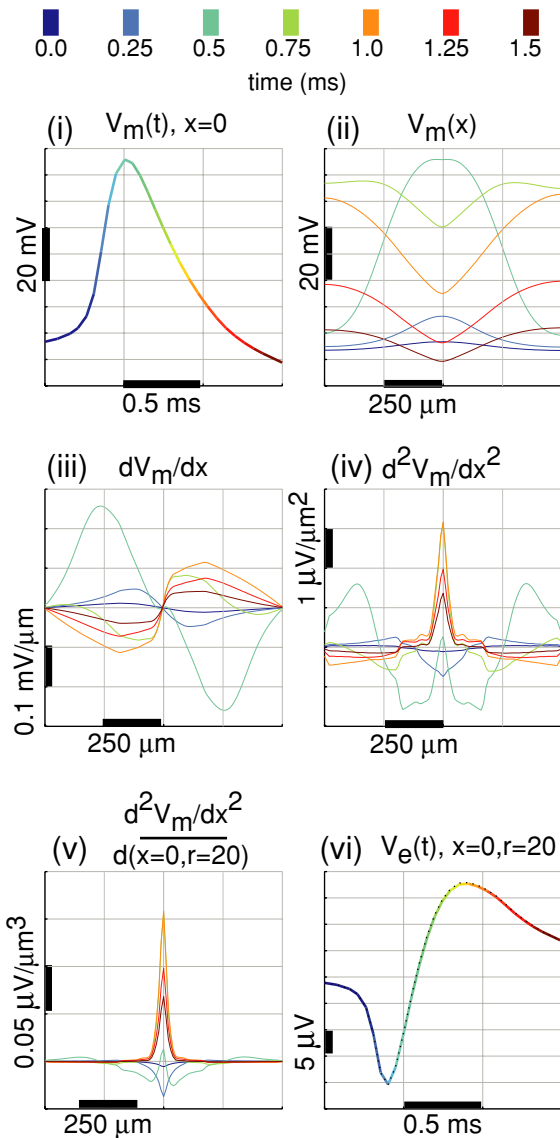


**Fig. 8**  $V_m$ , spatial derivatives of  $V_m$ , and  $V_e$  for a long cylinder model based on simulation (B). (i)  $V_m(t)$  at the center of the cylinder; (ii)  $V_m(x)$  at different times during the simulation, according to the color coded time scale: The action potential initiates in the center of the cylinder and then spreads at nearly full strength to both ends. Note that the  $x$ -axis scaling is shown in terms of distance, not in terms of the compartment index; (iii)  $dV_m/dx$ : Note that the center of the cylinder is defined as  $x = 0$  leading to the opposite sign for the first derivative on either side of the center; (iv)  $d^2V_m/dx^2$ ; (v)  $d^2V_m/dx^2$  scaled by distance, as in Eq. (7), for a location aligned with the center of the cylinder ( $x = 0$ ) at a radial distance of  $20 \mu\text{m}$  ( $r = 20 \mu\text{m}$ ). After  $d^2V_m/dx^2$  is scaled by the distance to a location  $V_e$  at any given time is the sum (or integral, in the continuous case) of  $d^2V_m/dx^2$  multiplied by a constant factor. While the AP is rising the second derivatives at the center is negative corresponding to the local maximum in  $V_m(x)$ . This leads to a negative  $V_e$ , corresponding to the  $\text{Na}^+$  dominant phase of the EAP. After the AP spreads the center is the minimum and the second derivative becomes positive. This leads to a positive  $V_e$ , corresponding to the  $\text{K}^+$  dominant phase of the EAP. (vi)  $V_e$  calculated with the approximate Eq. (7) (color) and the LSA (dotted line). For this simplified geometry, the two are indistinguishable

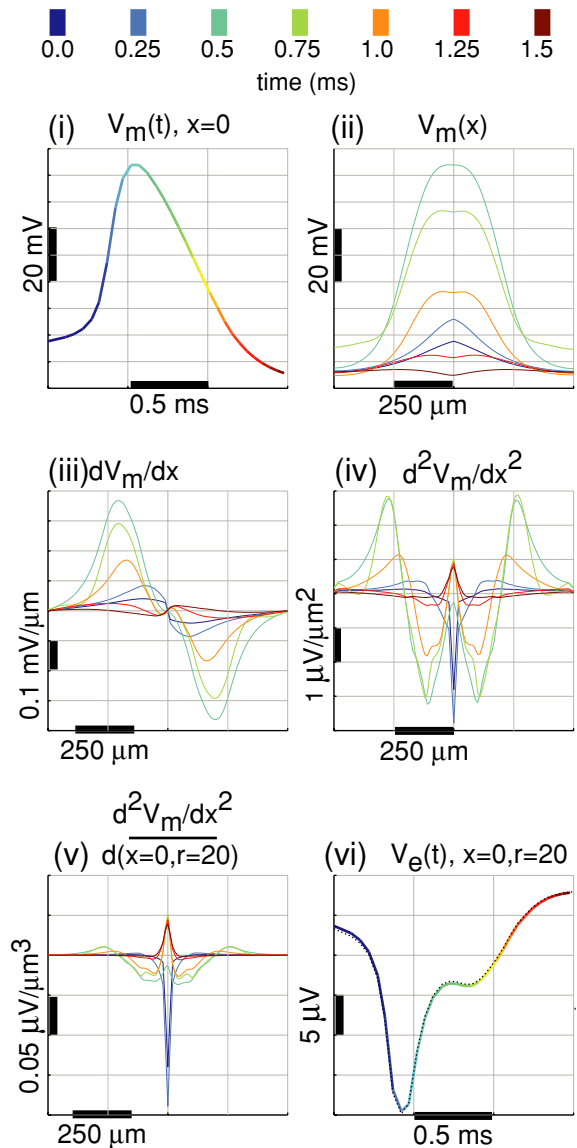


**Fig. 9**  $V_m$ , spatial derivatives of  $V_m$ , and  $V_e$  for a long cylinder model based on simulation (C). For a general description (see Fig. 8). After initiating at the center of the cylinder the action potential fails to propagate to the far ends of the cylinder. The second derivatives are most negative during the early rise of the AP and becomes less negative as the AP spreads, to the extent that it does, and the amplitude begins to fall. The amplitude at the center is not less than in surrounding cylinder until late in the AP and consequently the second derivative and  $V_e$  stay negative for longer than in simulation B. The inflection point, or pause, in the repolarization corresponds to a time when the spatial extent of the AP is narrowing just as the peak declines: the narrowing of spatial extent of the depolarization and flattening of distal voltages tends eliminate positive contributions to the second derivative, just as the falling amplitude is reducing negative contributions. This coincides to the inactivation of the A type  $\text{K}^+$  current, after it has blocked the backpropagation of the action potential. At the end of the process the center of the cylinder is finally somewhat hyperpolarized relative to the rest, due to the localized presence of the C current. This makes net positive second derivatives in the center of the cylinder, corresponding to the small amplitude  $\text{K}^+$  dominant phase

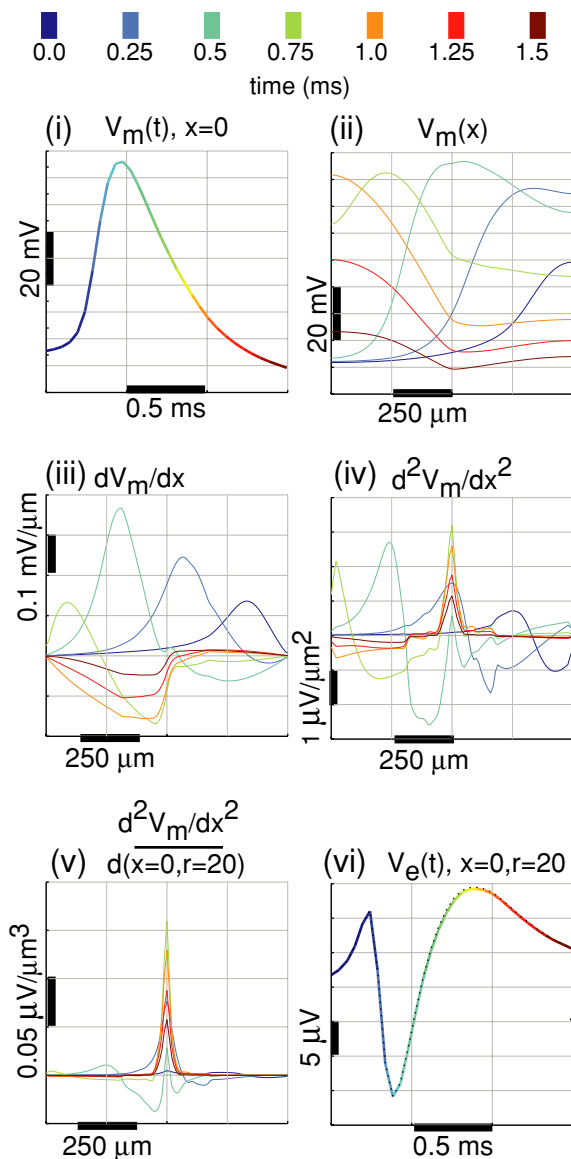


**Fig. 10**  $V_m$ , spatial derivatives of  $V_m$ , and  $V_e$  for a long cylinder model based on simulation (D). For a general description, see Fig. 8. The action potential initiates at one end of the cylinder and propagates to the far end. When the action potential initiates at the end of the cylinder  $V_m$  at the center of the cylinder begins to rise and the second derivative is positive, corresponding to the capacitive phase of  $V_e$ . As the rising phase of the AP passes the center of the cylinder the second derivative crosses zero and goes negative, corresponding to the maximum  $V_m$  at the center and the  $\text{Na}^+$  dominant phase of the EAP. The passage of the repolarizing slope of the AP causes another zero crossing of the second derivative and a return to positive values of  $V_e$ , corresponding to the  $\text{K}^+$  dominant phase of the EAP

we view  $V_e$  as a local measure that reflects the global pattern of activation. While considering the spatial gradients of  $V_m$  do not allow direct conclusions about the active conductance densities, this approach provides a more rigorous basis for understanding why such conclusions are possible.

### 3.5 Impact of conductance density noise

The second derivative is a mathematically ill-conditioned operation. It therefore has the property of amplifying any noise. This raises the question of whether the EAP remains useful for estimating active conductance densities in the case that they are perturbed by noise from constant or continuously varying values. That there is variability in the conductance density is suggested by patch clamp results (see e.g. Hoffman et al., 1997), but it is difficult to say how variability at the level of a patch translates into variability at the level of a compartment which is much larger. We assessed the impact of noise in the conductance densities by repeating the simulations of Sections 3.1 and 3.4 with the  $\bar{g}$  value for every conductance a random variable in every compartment except the soma. Somatic conductances were left fixed: the assumption of the model is that the soma provides the “true” base value for conductances in the rest of the neuron which follow noisy rules to determine the local densities.

The  $\bar{g}$  value for each conductance in each compartment was chosen separately from a uniform distribution having a minimum of 50% and a maximum of 150% of the value used for the fixed conductance simulation. That is,  $\bar{g} = \hat{g} + \hat{g} \times U(-0.5, 0.5)$ , where  $\hat{g}$  is the values for  $\bar{g}$  determined by the rules described in Gold et al. (2006a), Appendix C, and the parameters in Table 3, and  $U(a, b)$  describes a uniform random variable with minimum  $a$  and maximum  $b$ . This gives each conductance density variable a standard deviation of approximately  $0.3\hat{g}$ . Note that the kurtosis for a uniform random variable is  $-6/5$ , indicating that the variance is due to frequent modest size deviations from the mean rather than infrequent large deviations (the kurtosis of a Gaussian is 0).

Figure 11 shows the results for 10 trials each of simulations based on the parameter sets (A–D) of Section 3.1. The experiments show that the overall shape of the waveform is consistent despite noise in the conductance densities. The greatest impact is in changes to the peak negative amplitude which results from the changes to the  $\text{Na}^+$  density in the thick, proximal dendrites and the axon.

Figure 12 presents details of a single trial of the long cylinder simulation of Fig. 8, Section 3.4 with noise in the  $\bar{g}$  values. Noise in the conductance densities does in fact lead to significant noise in  $dV_m/dx$  and  $d^2V_m/dx^2$ . This suggests that the smoothly varying values for  $d^2V_m/dx^2$  (and the membrane current) in the simulations of Figs. 8–10 is due to the imposition of constant or continuously varying conductance densities. Nevertheless, because the noise in the conductance densities is uncorrelated from compartment to compartment, it tends to cancel out and results in only minor changes to the EAP measured at the center of the cylinder. Results for simulations of cylinders based on parameter sets (C) and (D) with noise in the conductance densities were similar.

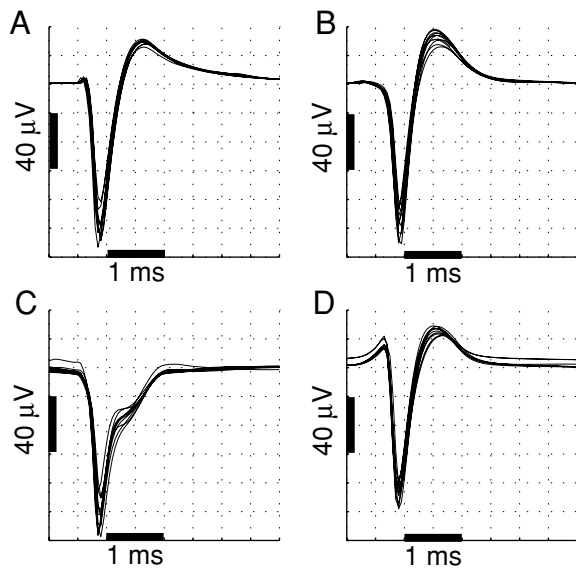


**Fig. 11** 10 examples of EAP's at a location near the soma for simulations (A)–(D) where the  $\bar{g}$  values for each conductance in each compartment except the soma is drawn from a random distribution with mean equal to the value for the original simulation. The waveform shapes remain very similar, although the amplitude of negative peak shows somewhat more variability than the overall waveform. The average peak weighted NSMSE values in comparison to the original simulation are: (A) 5.2%, (B) 3.4%, (C) 5.5%, and (D) 6.2%.

These results suggest that the EAP is a reliable indicator of the average distribution of conductance densities even if there is considerable variability from compartment to compartment. The biggest difficulty is in estimating the  $\text{Na}^+$  conductance density for the perisomatic region from the peak negative amplitude, a measurement we have already noted as ambiguous due to the presence of various fast  $\text{K}^+$  currents which may counteract the peak  $\text{Na}^+$  current. As will be discussed below, this measurement is made more ambiguous if the location of the electrode and the morphology of the neuron are unknown as in the case of modeling from *in vivo* EAP recordings.

### 3.6 Constraining distal conductances

We found that it was straightforward to create multiple simulations with different active conductance densities but similar somatic IAP's. At the same time, we found that it was much more difficult to create simulations with different conductance densities but similar EAP's. An example of this is shown in Fig. 13. The first of these two simulations is (B); the second is identical except that it has a maximal M type  $\text{K}^+$  conductance density of  $20 \text{ mS/cm}^2$ , rather than  $4.5 \text{ mS/cm}^2$  (see Table 3). In this case the IAP at the soma is altered by the conductance density change much more so than the EAP: the error between the two IAP traces is 9.8%, while the error between the two EAP traces is 5.0%. The errors at the distal

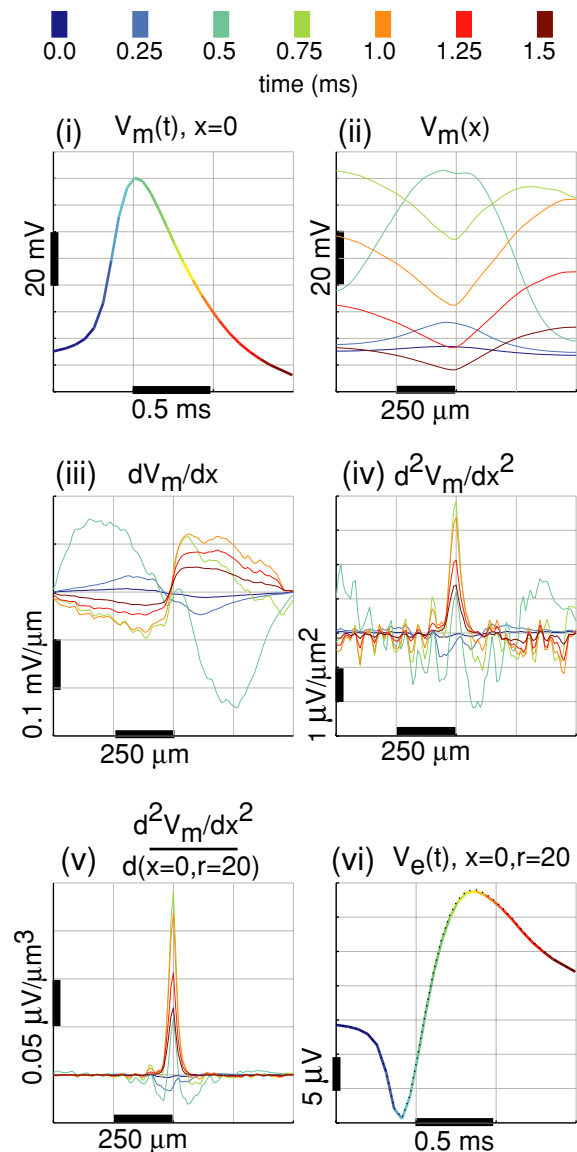


**Fig. 12**  $V_m$ , spatial derivatives of  $V_m$ , and  $V_e$  for a long cylinder model based on simulation (B), but with  $\bar{g}$  in every compartment a uniform random variable ranging from 50% to 150% of the value used in the simulation of Fig. 8. For a general description see Fig. 8. The action potential no longer propagates uniformly to both ends of the cylinder. Both  $dV_m/dx$  and  $d^2V_m/dx^2$  are no longer smooth functions, but rather show significant local variability. Nevertheless, because the variability at different locations is uncorrelated the summation over  $(1/d(x))d^2V_m/dx^2$  still yields an EAP waveform that is very similar to that for the simulation of Fig. 8

locations considered in Fig. 3 are similar for both EAP and IAP.

The reason for this result is that the M type  $\text{K}^+$  conductance has a much lower threshold of activation than the K type; for review see (Borg-Graham, 1999; Gold et al., 2006a) for details of the formulation used. Consequently the M type  $\text{K}^+$  conductance makes the largest contribution to repolarization in the distal dendrites where the IAP amplitude is small

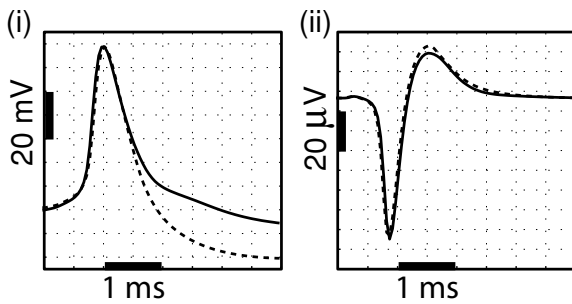


**Fig. 13** Comparison of intra and extracellular action potentials for two models with different M type  $K^+$  conductance densities. The first simulation (solid line) is Simulation (B) (Fig. 5). The second simulation (dashed line) is identical, except that the maximal M type  $K^+$  conductance density ( $\bar{g}$ ) is 20 mS/cm<sup>2</sup>, instead of 4.5 mS/cm<sup>2</sup>. (i) IAP at the soma. (ii) EAP measurements near the soma. The difference between the two conductance densities is more clearly observable in the IAP

and the K type  $K^+$  conductance is not strongly activated. (e.g., see Fig. 5(i), second row, last column). The result is that the proximal  $K^+$  currents are only slightly altered by the increase in M type  $K^+$  conductance and there is little change in the EAP near the soma or apical trunk. However, the net affect of the M type conductance in the distal dendrites leads to a much larger AHP.

This example illustrates the fact that for some differences in distal conductance densities the IAP can be a better measure of error than the EAP. However, in experiments where we made similar alterations to the distal A type  $K^+$  and the distal  $Na^+$  conductance densities there were still larger changes in the EAP than in the IAP. This suggests that for biologically plausible conductance density distributions this example may be the exception rather than the rule. This leads us to conclude that in general the EAP is probably a better model constraint than the IAP even for distal conductance densities. Changes in conductance densities in the soma and proximal dendrites always led to larger changes in the EAP than in the IAP.

### 3.7 Dependence of EAP waveform on electrode position

A serious potential liability of using  $V_e$  to tune a compartmental model is the dependence of the EAP on the precise electrode position, which was held constant in Fig. 3 and Table 2. One affect of position is that the amplitude of  $V_e$  declines with distance from the sources. In fact, the linear decrease in amplitude with distance in Eq. (3) underestimates the true impact: because the net membrane current summed over the entire neuron is always zero, an amplitude estimate derived from the isolated point source will overestimate the true amplitude from the closed source loop (De N6, 1947). The presence of equal and opposite positive and negative sources make a neuron similar to a dipole (Jackson, 1962) or

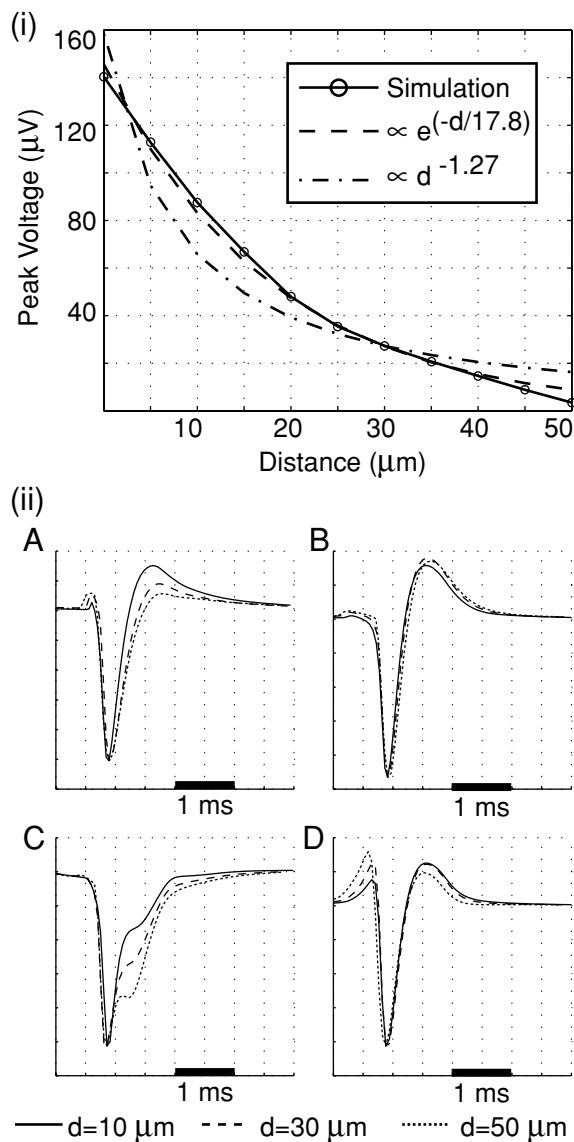
more accurately a tripole, also known as a linear quadrupole (Schwarz, 1973): in the depolarizing phase of the action potential the basal and apical dendrites form two positive poles and the soma is a negative pole of equal amplitude to the two positive poles combined. During repolarization, the polarity is reversed. At distances much large than the separation between the poles the amplitude of the voltage declines with distance squared for the dipole and with distance cubed for the tripole. These observation explain the bounds on the exponent,  $1 < b < 3$ , for the distance term in the denominator of Eq. (6).

However, neuronal measurements are typically made at distances of the same order of magnitude as the distance between the poles. We analyzed the decay of amplitude with distance from the cell body for a variety of cell morphologies and parameter sets. In these experiments we varied the position of the measurement in a direction perpendicular to the apical trunk so as to minimize the effect of proximity to any basal or oblique dendrites. The results, illustrated in Fig. 14, show that the decay in amplitude is close to distance to a power of  $-1.2$  at ranges of less than 50  $\mu\text{m}$  from the cell. A somewhat better fit is with an exponential decay having a length constant close to 20  $\mu\text{m}$ . At these distances and moving perpendicular to the apical trunk the waveform stays reasonably consistent in shape, although it does tend to widen as previously observed in Gold et al. (2006a).

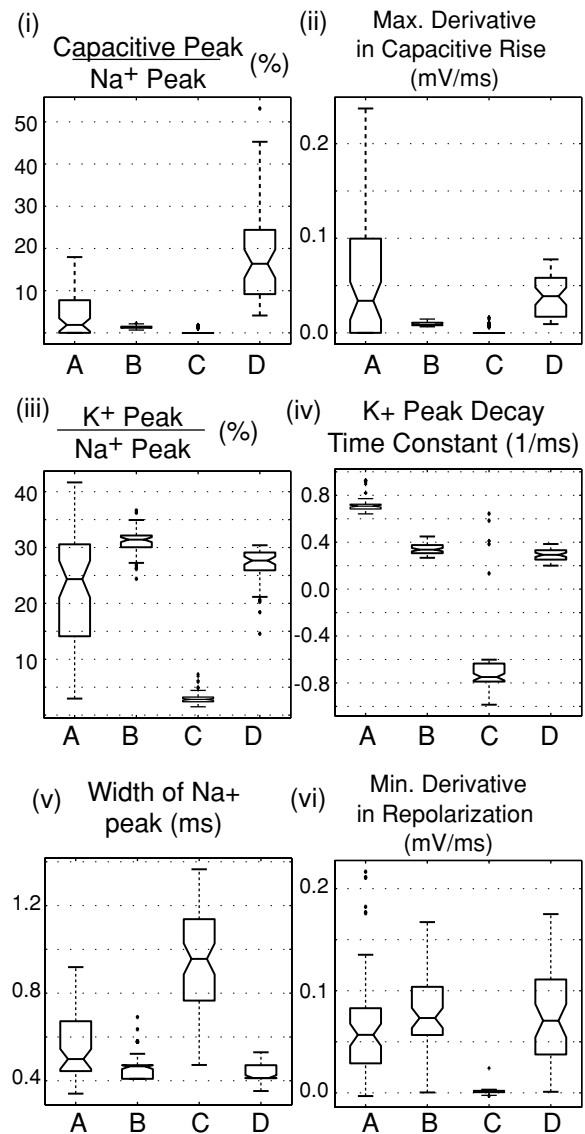
We also considered the variability in waveform shape that occurs with proximity to the basal and apical dendrites. We have already observed the increase in capacitive phase peak along the apical trunk in Section 3.1 and Gold et al. (2006a). The variability of waveform shape over a wide range of positions is analyzed in Fig. 15. This analysis compares measurements of the EAP shape that normalize for amplitude, as described in Section 2.5, for the four simulations of cell D151.

Figure 15(i) shows that while the large capacitive peak amplitudes in simulations (A) and (B) vary with position around the neuron, it is still a consistent distinguishing feature in comparison to (B) and (C). Although the distribution of amplitudes overlap the amplitude for (D) is consistently greater than the amplitude for (A). We also looked at the maximum first derivative of the waveform during the rise phase to see if the difference between the rise times to the capacitive peak is a consistent features. Figure 15(ii) shows that (A) displays faster rise times to the capacitive peak than (D), but the distributions are significantly overlapping and the means are similar. Still, when the two measures of the capacitive current peak are combined it seems that the difference between the rise time and peak amplitude of the capacitive peaks in simulations (A) and (D) is a consistent feature of the EAP's.

Figure 15(iii) compares the amplitude of the  $K^+$  current peak in the EAP's. It demonstrates that the lack of a well



**Fig. 14** Change in EAP amplitude and shape as a function of position. (i) Amplitude vs. distance in a line of points moving perpendicular to the apical trunk starting at the soma, along with best fits of exponential and power functions (amplitude refers to the amplitude of the negative peak), for cell D151 with parameters (B); the plot for other cells and parameter sets is similar. For parameter sets A–D and the 17 cell morphologies described in Section 3.8, the average length constant for the exponential decay fit is  $20 \mu\text{m}$  (std. dev =  $3 \mu\text{m}$ ), and the average exponent in the power function is  $-1.2$  (std. dev =  $0.1$ ). (ii) Comparison of the normalized waveform at positions 10, 30 and  $50 \mu\text{m}$  from the soma, also perpendicular to the apical trunk. The waveform tends to widen with distance, while its shape remains similar



**Fig. 15** Measurement of EAP Waveforms. For description of the measurements see Section 2.5 and Fig. 2. Figures show box plots for the measurements of EAP's in a  $100 \times 100 \mu\text{m}$  region around the soma spaced on a  $10 \mu\text{m}$  grid. Only EAP's with peak amplitude  $>40 \mu\text{V}$  were included in the statistics. The boxes have lines at the lower quartile, median, and upper quartile values. The lines extending from each end of the boxes ("whiskers") show the extent of the rest of the data. Outliers are data with values beyond the ends of the whiskers. The notches represent an estimate of the uncertainty about the medians for box-to-box comparison. \* (i) Ratio of capacitive peak to Na<sup>+</sup> peak. (ii) Maximum of the first derivative during the rise to the peak of the capacitive current phase. (iii) Ratio of K<sup>+</sup> peak to Na<sup>+</sup> peak. (iv) Decay time constant fit to the K<sup>+</sup> peak. "Negative" decay time constant indicates that there is no K<sup>+</sup> peak and that the waveform is rising during the period of the measurement. (v) Width of Na<sup>+</sup> peak at 25% of peak amplitude. (vi) Minimum of the derivative during repolarization of the Na<sup>+</sup> dominant phase. \*Statistical analysis performed with Matlab<sup>TM</sup> Statistics Toolbox

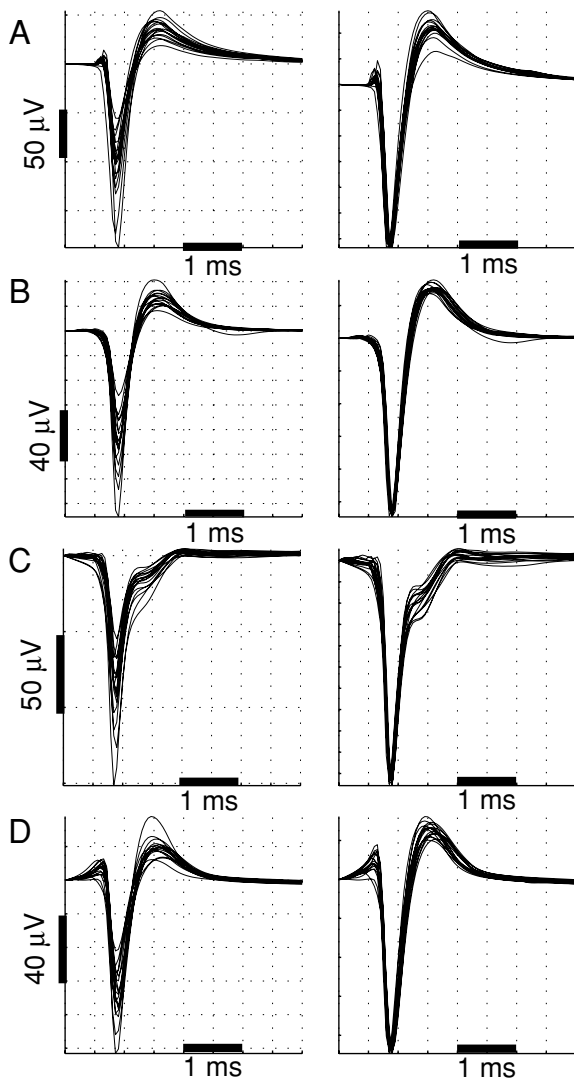


**Fig. 16** Comparison of simulations for varying cell morphology. *Left column:* EAP waveforms simulated near the soma for 17 reconstructed CA1 pyramidal neurons using parameter sets A–D. *Right column:* The same EAP waveforms normalized by the peak amplitude. The difference in cell morphology has a strong impact on the amplitude of the EAP, but the waveform shape is only slightly affected

defined  $K^+$  peak for (C) distinguishes it at all locations. However, the wide range of  $K^+$  peak amplitudes for (A) suggests that this is not a particularly useful criteria for distinguishing (A) and (B). The reason for the wide variation in the amplitude of the  $K^+$  peak for (A) is that the C type  $K^+$  conductance which dominates the repolarization is entirely concentrated at the soma. Thus an electrode near the soma will see a high amplitude  $K^+$  peak while an electrode closer to the dendrites will see a much smaller  $K^+$  peak. More useful is the time constant of the decay from the  $K^+$  peak, illustrated in Fig. 15(iv); in this measure the simulations (A) and (B) are completely non-overlapping and (C) is also easily distinguishable: (A) has the slowest time constant of decay owing to the slow decay of the C type  $K^+$  conductance, (B) has

a faster decay resulting from the rapid de-activation of the K type  $K^+$  conductance. Simulation (C) on the other hand typically has a “negative” time constant for the decay, indicating that the membrane potential is increasing in this period.

Another feature distinguishing (C) is the width of the  $Na^+$  peak. As illustrated in Fig. 15(v) the width of the  $Na^+$  peak for (C) is consistently different from (A) and (B), although slightly overlapping with (A). The distribution of widths for simulations (A), (B) and (D) seem to overlap too much for this to be a useful feature to distinguish them at an arbitrary location. Another useful measure for distinguishing (C) is the minimum first derivative during the repolarization phase, Fig. 15(vi). A low value for this measure indicates the presence of an inflection point in the repolarization of the EAP.

These results demonstrate that the main features distinguishing EAP waveforms are reasonably consistent throughout the region around a neuron where the amplitude is great enough to record with an extracellular electrode. Although any one feature does vary with position, taken in combination these features form consistent signatures that distinguish waveforms produced by different active conductance densities and different sequences of AP initiation.

### 3.8 Dependence of EAP waveform on cell morphology

Another potentially confounding factor in using EAP recordings to tune a compartmental model under an *in vivo* protocol is uncertainty regarding the morphology of the cell being recorded from. We performed simulations using the parameters of Table 3 on 16 additional reconstructed morphologies from Henze et al. (2000). The results are illustrated in Fig. 16. The difference in cellular morphology has a very strong impact on the amplitude of the measured waveform: the difference between the smallest amplitude and largest amplitudes is around a factor of three for each parameter set. However, for the same membrane conductance densities and initiation conditions the shape of the waveform stays consistent. We previously demonstrated in Gold et al. (2006a) that even using the morphology of a non-pyramidal cell leads to the same result: a change in the EAP amplitude but little change in the EAP waveform shape. In our ongoing experiments on cortical neurons (Gold et al., 2006b) we have found the same rule holds for the wider range of neuronal morphologies found in cortex: morphology primarily influences EAP amplitude, while the balance of active conductances and pattern of AP initiation determines EAP shape.

The impact of neuron size on EAP amplitude is more precisely illustrated in Fig. 17 which plots peak amplitude as a function of cell size for the 17 cells and 4 parameter sets. The largest cells in the set is around around twice the size of the smallest: The total length of the dendrites range from 7000 to 13,000  $\mu\text{m}$  (average 10,200  $\mu\text{m}$ ), and

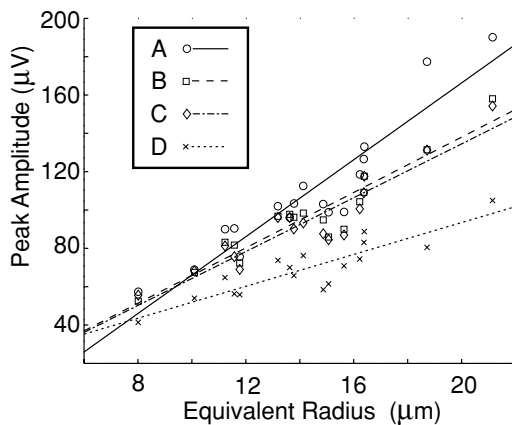


**Fig. 17** Peak amplitude of the negative peak vs. cell size for the 4 parameter sets. Cell size is plotted as the radius of a sphere with the same surface area as the soma and apical trunk out to the first branch point for each cell. For these cells the combined soma + apical surface area ranges from 300 to 2000  $\mu\text{m}^2$ . For the data sets A–D the correlation co-efficient between size and amplitude are 0.94, 0.94, 0.93 and 0.88,  $p < 1e-6$ . Lines fit to each set of points have slopes of 10, 7, 7 and 4  $\mu\text{V}/\mu\text{m}$  for parameters sets A–D respectively

the total surface areas for the soma and dendrites combined ranges from 15,000 to 28,000  $\mu\text{m}^2$  (average 22,000  $\mu\text{m}^2$ ). The measure which we found most closely correlated to the amplitude of the EAP waveform was the combined surface area of the soma and proximal apical trunk (out to the first branch point). This is because, with conductance *densities* being equal, the total current scales with surface area. The soma and apical trunk make up the largest amount of surface area that can be within range of a recording electrode: While the finely branched distal dendrites make up much of the surface area of a CA1 pyramidal neuron, they are too dispersed in space to make a significant extracellular potential.

#### 4 Discussion

These results illustrate the fact that single compartment  $V_m$  measurements under-constrain realistic compartmental models that include non-uniform active conductance densities. Because the EAP waveform is more sensitive to the precise composition of the active ionic conductances, it may provide a suitable means for constraining a compartmental model despite the uncertainty arising due measurement location. An alternative viewpoint of the situation is provided by the relationship between  $V_e$  and the second spatial derivative of  $V_m$ : the second spatial derivative is sensitive to the overall pattern of activation in the neuron, while the membrane potential waveform in a single compartment is much less so.

That said, it is not true that  $V_m$  contains no information about the overall pattern of activation. Close observation

of the early rising phase of the AP and the slope during the repolarization phase provide some of the same clues as do measurement of  $V_e$ . But standard measurements of  $V_m$ , such as the amplitude and duration of the peak and amplitude of the AHP, are insensitive to these subtleties and it is these gross features that dominate an MSE based objective function. This explains the relatively superior performance of objectives functions involving time derivatives of  $V_m$  (Hayes et al., 2005). The advantage of using  $V_e$  measurements is that its dependence on  $V_m''(x)$  amplifies subtle differences and gives them a more prominent role in a MSE objective function.

The problem with  $V_m$  measurements can be mitigated if additional measurements of the IAP are made at multiple, distal locations (i.e.  $>200 \mu\text{m}$  from the soma). These findings agree with those of Keren et al. (2005), who used genetic algorithms to tune compartmental models. They suggested using multiple membrane potential recordings in the axon and dendrites in order to best constrain the model parameters. Huys et al. (2006) take this approach to its logical conclusion: if the membrane potential is known for all compartments of a neuron then optimal parameters can be calculated by linear regression without resorting to a search of the parameter space. In practice, however, performing multiple  $V_m$  measurements on the same cell is difficult *in vitro* and presently impossible *in vivo*. Voltage imaging technologies also need maturation before the measurements proposed by Huys et al. (2006) become routine and sufficiently accurate. Our results suggest that using extracellular recordings may be an attractive alternative. At the present time, EAP recordings are not routinely made during *in vitro* experiments designed to analyze the properties of active ionic conductances. However, EAP recordings may provide significant additional information in such a context.

*In vivo* protocols, it is often the case that EAP recordings are the only data available. The results presented in Sections 3.7 and 3.8 demonstrate that variation in morphology and electrode position primarily affect the amplitude of the EAP waveform, but not the EAP waveform shape. This uncertainty over amplitude adds uncertainty due to natural variation in conductance densities throughout a neuron, as suggested in Section 3.5. We conclude that a useful approach to constraining a model from *in vivo* data would be to make a model reproduce the features of the EAP waveform *shape(s)* while allowing some freedom in EAP amplitude.

In order to use EAP waveform shapes to tune a model, the individual spikes for each clustered unit must be averaged to produce a low noise average waveform. These can be analyzed and statistics similar to those described in Section 3.7 can be calculated. Such statistics can be compared to the average measurements from the simulation where the average is taken over both the unknown electrode position and a range of plausible morphologies. Alternatively, the

recordings can be normalized and clustered (a second time) to search for prototype shapes in the extracellular recordings. Each prototype shape would suggest a different combination of active conductances or pattern of action potential initiation that may exist side by side in the target neuron population.

At the same time, it can and should be verified that the tuned model reproduces the *range* of EAP amplitudes observed in recordings. In particular, the largest cells in the morphology sample should be able to reproduce the highest amplitude EAP recordings under the assumption of a plausible extracellular resistivity and electrode location. Gold et al. (2006a) and Section 3.7 demonstrated that the Na<sup>+</sup> dominant phase of an EAP waveform tends to widen as the electrode is moved away from a neuron. But given the high intrinsic variability in waveform width (e.g. Fig. 15(v)) there is no way of knowing for certain whether a low amplitude EAP recorded *in vivo* comes from a near measurement of a small cell or a distant measurement of a large cell. Therefore, it seems somewhat less useful to check that a model reproduces low amplitude EAP recordings.

These methods will constrain the parameters to plausible ranges, not determine a single “best” value. This is an appropriate approach to *in vivo* modeling: our own experience modeling *in vivo* recordings (Gold et al., 2006a) as well as studies of gene expression (Toledo-Rodriguez et al., 2004) suggest that the active conductance densities for neurons *in vivo* are highly variable. Therefore, any modeling result should be tested over a range of plausible conductance densities to determine the parameter sensitivity. Because of the insensitivity of waveform shape to both position and morphology we believe that this method would give very useful results for any part of the central nervous system, and not only the CA1 region of Hippocampus that we have studied here.

When analyzing EAP waveforms recordings should be wide band filtered, 1 Hz–3 kHz or 5 kHz. While bandpass filtered data must usually be used to detect and cluster spikes, average waveform shapes can be created from the wide-band after spike times have been determined. Typical bandpass filter settings used for unit detection and spike sorting (i.e. ~300 Hz–~1 kHz) lead to significant distortion of the waveform shape. Multi-site silicon probes seem preferable to tetrodes as they allow precise knowledge of the relative position of the recording sites. Our experiences in Gold et al. (2006a) suggest that this gives a much tighter constraint on the parameters.

In Section 3.7 we concentrated on simple and intuitive measurements of the waveform. But more sophisticated means for measuring waveform attributes could be developed; for example, using wavelet decompositions (e.g. Quiroga et al., 2004). A related subject that warrants further research is how these types of measurements may change for a single neuron under various conditions such as high firing rate, LTP or influence of neuromodulators. Such knowledge

could help to improve clustering algorithms for chronic *in vivo* recordings that must track units over many days and under different conditions.

This study focused on constraining the conductance density of active ionic channels and the conditions of action potential initiation. But the sensitivity of the EAP to changes in the membrane current should also make it suitable for constraining the kinetics of active conductances as well. The contribution of the (positive) capacitive current to the EAP suggests that EAP's may be useful for tuning the membrane capacitance. However, in practice the membrane capacitance is well established (Koch, 1999) and probably does not vary between individual neurons. Our results suggest that the EAP may be somewhat less useful in tuning the resting leak conductance. For this purpose, sub-threshold measurements of the membrane potential probably remain the most useful technique (e.g. Spruston and Johnston, 1992).

In the experiments described in Gold et al. (2006a), we found that intracellular resistivity,  $R_i$  (which determines the individual  $R_a$  values based on compartment size), actually had a significant impact on the *amplitude* of the EAP peak. From the point of view of membrane currents, this is because of the role of  $R_a$  in determining the input resistance and how much Na<sup>+</sup> current is required to achieve a given peak IAP amplitude. Equation (7) demonstrates the importance of  $R_a$  for the extracellular potential in terms of the second derivative of the membrane potential. Therefore, simultaneous IAP and EAP measurements at known locations seem to have some value for constraining  $R_i$  based on the peak EAP amplitude.

To facilitate further research, we have created a down-loadable package of all the NEURON and Matlab code used to perform the experiments described in this study. The code can easily be extended to simulate EAP's from compartmental models of any type of neuron. It is available from the ModelDB on the Internet at <http://senselab.med.yale.edu/SenseLab/ModelDB/ShowModel.asp?model=84589>.

**Acknowledgments** We would like to thank György Buzsáki for allowing the use and publication of the CA1 pyramidal cell morphology D151 (Henze et al., 2000) and for many helpful discussions. This work was supported by National Institute of Mental Health (NIMH) Fellowship 1-F31-MH-070144-01A1 and Grant MH-12403, National Institute of Neurological Disorders and Stroke Grants NS-34994 and NS-43157, the NIMH-supported Conte Center for the Detection and Recognition of Objects, and the National Science Foundation.

## References

- Bédard C, Kröger H, Destexhe A (2006) Model of low-pass filtering of local field potentials in brain tissue. *Phys. Rev. E* 73: 051911.

- Borg-Graham LJ (1999) Interpretations of data and mechanisms for hippocampal pyramidal cell models. *Cerebral Cortex* 13: 19–138.
- Buzsáki G, Kandel A (1998) Somadendritic backpropagation of action potentials in cortical pyramidal cells of the awake rat. *J. Neurophysiol* 79(3): 1587–1591.
- Colbert CM, Magee JC, Hoffman DA, Johnston D (1997) Slow recovery from inactivation of Na<sup>+</sup> channels underlies the activity-dependent attenuation of dendritic action potentials in hippocampal CA1 pyramidal neurons. *Neuroscience* 17: 6512–6521.
- Colbert CM, Pan E (2002) Ion channel properties underlying the axonal action potential initiation in pyramidal neurons. *Nat. Neurosci.* 5(6): 533–538.
- De N6 RL (1947) Action potential of the motoneurons of the hypoglossus nucleus. *J. Cell Comp. Physiol.* 29: 207–287.
- Forsyth DA, Ponce J (2003) *Computer Vision: A Modern Approach*. Prentice Hall, Saddle River, NJ.
- Gold C, Henze DA, Koch C, Buzsáki G (2006a) On the original of the extracellular action potential waveform: a modeling study. *J. Neurophys.* 95: 3113–3128.
- Gold C, Girardin C, Martin K, Koch C (2006b) Unpublished experiments.
- Hayes RD, Byrne JH, Cox SJ, Baxter DA (2005) Estimation of single-neuron model parameters from spike train data. *Neurocomputing* 66: 517–529.
- Henze DA, Borhegyi Z, Csicsvari J, Mamiya A, Harris K, Buzsáki G (2000) Intracellular features predicted by extracellular recordings in the hippocampus *in vivo*. *J. Neurophysi.* 83: 390–400.
- Hines ML, Carnevale NT (1997) The neuron simulation environment. *Neural Comput.* 9: 1179–1209.
- Hines ML, Carnevale NT (2001) *Neuron: A tool for neuroscientists*. *The Neuroscientist* 7: 123–135.
- Hoffman DA, Magee JC, Colbert CM, Johnston D (1997) K<sup>+</sup> channel regulation of signal propagation in dendrites of hippocampal pyramidal neurons. *Nat. Neurosci.* 387: 869–875.
- Holt G (1998) A Critical Reexamination of Some Assumptions and Implications of Cable Theory in Neurobiology. PhD thesis, California Institute of Technology.
- Holt G, Koch C (1999) Electrical interactions via the extracellular potential near cell bodies. *J. Comput. Neurosci.* 6: 169–184.
- Huys, QJM, Ahrens MB, Paninski I (2006) Efficient Estimation of Detailed Single-Neuron Models *J Neurophys.* 96: 872–890.
- Jackson JD (1962) *Classical Electrodynamics*. Wiley, New York.
- Keren N, Peled N, Korngreen A (2005) Constraining compartmental models using multiple voltage recordings and genetic algorithms. *J. Neurophysio.* 94: 3730–3742.
- Klee R, Ficker E, Heinemann U (1995) Comparison of voltage-dependent potassium currents in rat pyramidal neurons acutely isolated from hippocampal regions CA1, CA3. *J. Neurophysiol.* 74: 1982–1995.
- Koch C (1999) *Biophysics of Computation*. Oxford University Press, Oxford, UK.
- Koch C, Segev I (Eds.) (1999) *Methods in Neuronal Modeling: From Ions to Networks*. Bradford, Cambridge, Massachusetts.
- L6pez-Aguado L, Ibarz JM, Herreras O (2001) Activity-dependent changes of tissue resistivity in the CA1 region *in vivo* are layer specific: modulation of evoked potentials. *Neuroscience* 108(2): 249–262.
- Magee JC, Johnston D (1995) Characterization of single voltage-gated Na, Ca<sup>2+</sup> channels in apical dendrites of rat CA1 pyramidal neurons. *J. Physiol.* 487: 67–90.
- Mainen ZF, Joerges J, Huguenard JR, Sejnowski TJ (1995) A model of spike initiation in neocortical pyramidal neurons. *Neuron* 15: 1427–1439.
- Malmivuo J, Plonsey R (1995) *Bioelectromagnetism*. Oxford University Press, New York, Oxford.
- Migliore M, Sheperd GM (2002) Emerging rules for the distributions of active dendritic conductances. *Nat. Rev. Neurosci.* 3: 362–370.
- Plonsey R (1969) *Bioelectric Phenomena*. McGraw-Hill, New York.
- Quiroga RQ, Nadasdy Z, Ben-Shaul Y (2004) Unsupervised spike sorting with wavelets and superparamagnetic clustering. *Neur. Comput.* 16: 1661–1687.
- Rall W (1962) Electrophysiology of a dendritic neuron model. *Biophys J.* 2: 145–167.
- Schwarz WM (1973) *Intermediate Electromagnetic Theory*. Robert E. Kreiger Publishing Company, New York.
- Spruston N, Johnston D (1992) Perforated patch-clamp analysis of the passive membrane properties of three classes of hippocampal neurons. *J. Neurophysiol.* 67(3): 508–529.
- Stuart G, Spruston N, Häusser M (2001) *Dendrites*. Oxford University Press, Oxford, U.K.
- Toledo-Rodríguez M, Blumenfeld B, Wu C, Luo J, Attali B, Goodman P, Markram H (2004) Correlation maps allow neuronal electrical properties to be predicted from single-cell gene expression profiles in rat neocortex. *Cerebral Cortex* 14(12): 1310–1327.
- Vanier MC, Bower JM (1999) A comparative survey of automated parameter search methods for compartmental models. *J. Comput. Neurosci.* 7(2): 149–171.
- Varona P, Ibarz JM, Lopez-Aguado L, Herreras O (2000) Macroscopic and subcellular factors shaping population spikes. *J. Neurophysiol.* 83: 2192–2208.